



# A Study of Intermittent Turbulence in Stable Arctic Boundary Layers

Brian J. Butterworth<sup>1,2</sup> · Gijs de Boer<sup>1,2,3</sup> · Dale Lawrence<sup>4</sup>

Received: 8 April 2023 / Accepted: 20 November 2023 / Published online: 12 January 2024  
© The Author(s) 2024

## Abstract

Polar boundary layers are difficult to model due to the existence of intermittent turbulence within stable layers. Here we present a case study evaluation of coherent structures in a stable boundary layer observed during a series of flights with an uncrewed aircraft system (Data-Hawk2) on 19 October 2016 at Oliktok Point, Alaska as part of the ERASMUS (Evaluation of Routine Atmospheric Sounding Measurements using Unmanned Systems) field campaign. During a sequence of five flights over a nine-hour period, 57 profiles of atmospheric properties (0–400 m a.g.l.) were collected. Turbulence was identified using derived Richardson Number, temperature structure function parameter, and turbulence kinetic energy dissipation. Throughout all flights on this strongly stable day, intermittent turbulence was observed. These turbulent layers showed well-mixed potential temperature profiles embedded within otherwise stable potential temperature profiles; often resulting in a characteristic staircase pattern. Turbulent layers ranged from 1 to 30 m deep, with most individual layers being 1–2 m deep. Vertical propagation velocities of layers in the lower atmosphere were on the order of a few  $\text{cm s}^{-1}$ , typical of non-convective environments. In different regions of the profile, turbulence was driven by a different balance of buoyancy and shear forces, with turbulence in the near surface environment driven by strong shear forces overcoming strong resistance to buoyancy, while turbulence in elevated layers characterized by weaker shear forces overcoming weaker resistance to buoyancy. We discuss the potential of such datasets for improving subgrid parameterizations of small-scale turbulence embedded within stable boundary layers.

**Keywords** Intermittent turbulence · Stable boundary layer · Uncrewed aircraft systems

---

✉ Brian J. Butterworth  
brian.butterworth@colorado.edu

<sup>1</sup> Cooperative Institute for Research in Environmental Sciences, University of Colorado Boulder, Boulder, CO 80309, USA

<sup>2</sup> Physical Sciences Laboratory, National Oceanic and Atmospheric Administration, Boulder, CO 80305, USA

<sup>3</sup> Integrated Remote and In Situ Sensing, University of Colorado Boulder, Boulder, CO 80309, USA

<sup>4</sup> Aerospace Engineering Sciences, University of Colorado Boulder, Boulder, CO 80303, USA

## 1 Introduction

The stable boundary layer (SBL) is one of the most poorly understood states of the atmospheric boundary layer (ABL; Fernando and Weil 2010). Nonetheless, it is a critically important condition of the lower atmosphere, responsible for fog formation, katabatic winds, and circulations in complex terrain. It also impacts human enterprises, as it can lead to frost damage, drive the buildup of high concentrations of contaminants, and significantly affect visibility. Unfortunately, adequate representation of the SBL by models is challenging because of the range of processes that influence its dynamics (e.g., radiation divergence, land surface coupling, orographic drag, and mesoscale motions, etc.) and their interactions (Steenefeld 2014). These processes result in intermittent turbulence that doesn't fit neatly into the physical frameworks of the convective boundary layer.

This intermittent turbulence presents one of the main challenges for modeling the SBL. Under very stable conditions turbulence becomes decoupled from the surface (Kaimal and Finnigan 1994)—a condition referred to as *z-less stratification* (Wyngaard and Coté 1972). The Monin–Obukhov (MO) similarity surface layer scaling that forms the basis of most ABL schemes in numerical weather prediction (NWP) models, while effective under convective and neutral conditions, is not effective under such decoupling (Couvreur et al. 2020). Nieuwstadt (1984) showed that MO similarity could be adapted for local scaling of elevated stable layers, but only for weakly stable conditions. There remains no well-established scaling between thermodynamic profiles and turbulence variables for very stable conditions (van de Wiel et al. 2012).

Improving flux-gradient relationships for SBLs is particularly important for improving atmospheric models because models are highly sensitive to parameterizations of the SBL (Holtslag et al. 2013). Currently, climate and NWP models inadequately represent SBLs in a range of ways, including biases in near-surface temperature, surface energy exchange, ABL depth, and ABL wind speed (Tjernström et al. 2005; Cuxart et al. 2006; Steeneveld 2014). Stability functions can be adjusted to have short-tailed or long-tailed distributions to disable or enable (respectively) mixing in grid cells with supercritical Richardson numbers. However, such manual adjustments aimed at reducing specific biases often result in enhancement of other biases (Tjernström et al. 2009; Sandu et al. 2013; Medeiros and Fitzjarrald 2014), emphasizing the need for more physically-based parameterizations of the various processes influencing turbulence in the SBL (Steenefeld 2014).

The development of improved model parameterizations leads to an additional complication: small scale. Mahrt (2014) shows that the morphology of coherent structures in the SBL is highly variable and distinct—with turbulent structures of smaller temporal and spatial scales than that observed in convective and neutral ABLs. Such small-scale turbulence (on the order of meters and seconds) is believed to be dynamically important within SBLs, as highlighted by previous observations (Nappo 1991; Muschinski and Wode 1998; Balsley et al. 2008; Tjernström et al. 2009) and direct numerical simulations (Fritts et al. 2009). However, under the space and time averaging required for operational models,  $\theta$  takes on a more uniform stable structure and the turbulence fails to be represented (Balsley et al. 2013; Sullivan et al. 2016). Therefore, SBLs also represent a subgrid parameterization problem. One that requires high resolution observations to address.

Observations of turbulent structures within SBLs have been made using towers (Sun et al. 2004; Nakamura and Mahrt 2005; Medeiros and Fitzjarrald 2014; Kral et al. 2021), ground-based remote sensing (Coulter 1990; Sun et al. 2004), tethered lifting systems (TLS; Balsley

et al. 2003, 2006; Meillier et al. 2008), high-resolution balloon measurements (Dalaudier et al. 1994), and aircraft (Mahrt 1985; Muschinski and Wode 1998; Dai et al. 2014).

In-situ tower measurements identify intermittent turbulence as temporal variability of vertical velocity—temporary pulses of high turbulence during predominantly stable conditions (Nakamura and Mahrt 2005; Costa et al. 2011; Medeiros and Fitzjarrald 2014; Kral et al. 2021; Allouche et al. 2022). Using a 7-tower eddy covariance array (positioned 100 and 300 m from a central tower), Nakamura and Mahrt (2005) show that intermittent turbulence within SBLs is constantly in some state of evolution or decay, with individual turbulence events often occurring at small temporal and spatial scales. They found that decaying turbulence observed at a single location could be due to advection from an upwind region with lower Richardson number (i.e., turbulent regions). Over a larger, regional tower network, Medeiros and Fitzjarrald (2014, 2015) showed that the intermittent turbulence characteristics at individual sites typically matched those projected by a regional Richardson analysis, but could deviate based on topography and surface heterogeneity. It was found that “not-so-cold-spots” with subcritical Richardson numbers could generate turbulent mixing over a landscape whose regional Richardson number was supercritical.

In addition to horizontal variability, turbulence characteristics can be influenced by the vertical structure of the SBL. Commonly, the lower atmosphere is separated into the SBL at the surface and a residual layer (RL) above it (where the remnants of the previous day’s ABL sits below a capping inversion separating it from the free troposphere; Balsley et al. 2003, 2008; Tjernström et al. 2009). In the SBL radiative cooling generates a stable temperature profile. This can extend all the way to the surface or sit slightly above. In the latter instance the SBL can be further divided into a shallow boundary layer at the surface with a quiescent layer immediately above (Banta et al. 2007). The shallow boundary layer acts like a conventional boundary layer, where turbulent mixing is generated by surface shear (Fernando and Weil 2010), while the quiescent layer is characterized by a strong inversion which inhibits turbulent mixing.

The strong near surface inversion of the SBL often creates a barrier between the surface and the atmosphere above, inhibiting upward transport of surface fluxes to the RL. However, even when the RL has stable thermal stratification, intermittent turbulence is often still present. This can be generated by wind shear from a variety of atmospheric processes, including low-level jets (LLJ), mesoscale motions, gravity waves, and density currents (Fritts et al. 2003; Mahrt and Vickers 2003). Such turbulence above a decoupling inversion can often create an “upside down” boundary layer, where turbulence is transported downwards (Mahrt 1999). While the extent of the turbulence is expected to be determined by the scale of the shear instability or wave breaking event (Fritts et al. 2003), the nature of how such intermittent turbulence evolves is still an unsettled question.

One promising new tool that provides a unique set of advantages for identifying turbulent characteristics in the ABL are uncrewed aircraft systems (UAS; van den Kroonenberg et al. 2012; Balsley et al. 2018; Kral et al. 2021) The high resolution of UAS measurements provides an ability to identify intermittent turbulence within profiles at the requisite small scales. They can fly higher than towers, can sample over multiple locations, and provide opportunities for both profiling and horizontal measurements. Additionally, the highly-adaptable flight patterns of these small platforms provide detailed perspectives on a specific area of interest—in this case a very strong inversion layer that had developed in the lower atmosphere overnight under clear skies.

In the current study, we conduct a case-study-based evaluation of coherent structures in a stable boundary layer, leveraging observations collected by a small UAS (DataHawk2; Hamilton et al. 2022). As part of the ERASMUS (Evaluation of Routine Atmospheric Sounding

Measurements using Unmanned Systems; de Boer et al. 2018) field campaign, the DataHawk2 UAS was operated at Oliktok Point, Alaska (70.51° N, 149.86° W), conducting a series of flights on 19 October 2016 with a focus on the strong stratification present between the surface and 200 m a.g.l. Data from these flights is analyzed in conjunction with data from other instrumentation to examine small-scale dynamics of the evolving lower atmosphere.

Here we identify and characterize coherent structures in SBLs from UAS profiling data. We attempt to understand how intermittent turbulence develops and propagates in SBLs and determine whether repeated profiling of basic meteorological variables can provide insight into the geophysical drivers of turbulence in SBLs. Specifically, we ask

- (1) Do we observe mixed-layers resulting from intermittent turbulence in the stable boundary layer?
- (2) What is the vertical extent of these layers of intermittent turbulence?
- (3) How are these layers propagating vertically and what is their propagation velocity?

We begin with an overview of the tools and methods used to produce the dataset (Sect. 2), including a case study overview, descriptions of the field site and the DataHawk2 UAS, and the analyses used to investigate turbulence in the SBL. Results from these analyses are provided in Sect. 3. Section 4 provides a discussion on how these UAS results fit into the previous research on intermittent turbulence in the SBL. Section 5 provides a summary and conclusions.

## 2 Methods

The ERASMUS campaign was carried out at Oliktok Point, Alaska, where the Sandia National Laboratories operated the third Department of Energy (DOE) Atmospheric Radiation Measurement (ARM) Mobile Facility (AMF-3) between the fall of 2013 and summer of 2021. The AMF-3 included a variety of instruments to document the state of the atmosphere, including surface-based in-situ observing systems for measuring surface meteorology, surface conditions, and precipitation properties, as well as remote sensors to measure cloud, precipitation, and wind characteristics. Additionally, instrumentation was included to measure aerosol and radiation properties at the site. Situated approximately 200 m from the Arctic Ocean (Fig. 1), the facility observes the coastal environment of the North Slope of Alaska, providing perspectives on marine and continental air-masses, depending on wind direction and synoptic state.

### 2.1 DataHawk2

As part of ERASMUS, in October 2016 a team from the University of Colorado Boulder (CU) traveled to Oliktok Point to deploy the DataHawk2 UAS to collect in-situ observations of the lower atmosphere during the fall freeze-up period. The DataHawk2 is a custom-built aircraft, designed and developed at CU primarily to support atmospheric science missions (Hamilton et al. 2022). This aircraft features a 1.2 m wingspan and weight of approximately 1.7 kg, including batteries. In its standard configuration, the aircraft has a flight time of approximately 1 h, carrying a variety of sensors to support atmospheric research. For ERASMUS, the aircraft was equipped with an interMet systems radiosonde sensor as the primary source of calibrated temperature and humidity information. The sensing element was mounted on the top of the aircraft body, extending into the free airstream flowing over the aircraft in flight. Additionally, the DataHawk2 carried a custom finewire array that includes both a hotwire for high frequency

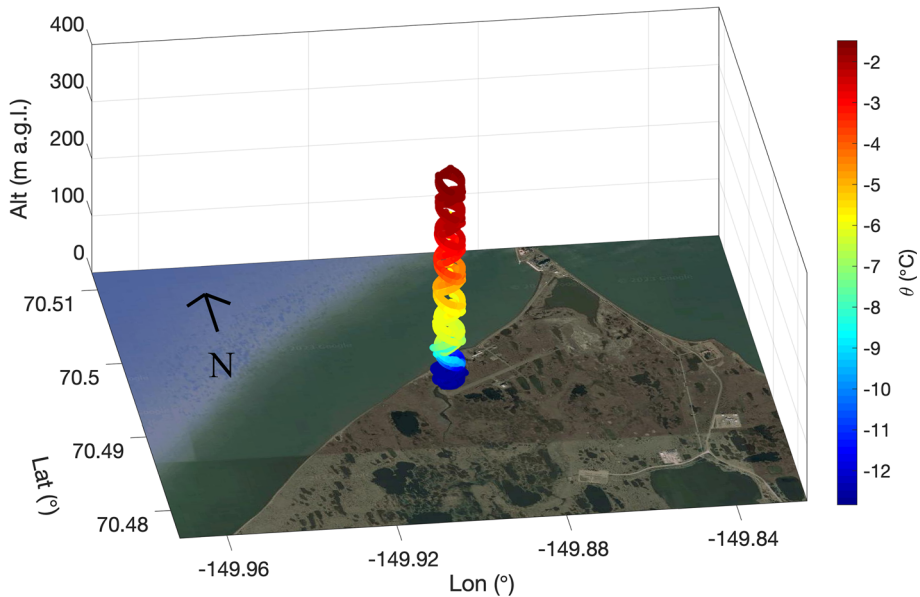


**Fig. 1** Three-dimensional potential temperature profile projected on a satellite surface map for Flight 1 (1726–1758 UTC on 19 October 2016). Flights occurred over the SW end of the runway 2.25 km SW of the point and roughly 200 m away from the ocean at their closest pass. Vertical dimensions are 4x exaggerated relative to surface dimensions to highlight the profile. (Map data: Google, TerraMetrics)

airspeed measurements, and a coldwire to provide very fast temperature information. These wires were accompanied by a SHT-85 temperature and humidity sensor used to calibrate the coldwire for each individual flight. A pair of IR thermopile sensors provided uncalibrated brightness temperatures of the region under and above the aircraft, allowing users to detect surface- and sky-cover gradients such as those resulting from the coastal interface or variable cloud cover. Finally, the onboard inertial measurement unit (IMU), global positioning system receiver (GPS), and onboard pitot tube together provided measurements necessary to estimate the horizontal wind speed and direction at the altitude of the DataHawk2's flight. More detail on these sensors and data recovery methods can be found in (Hamilton et al. 2022). Data collected during ERASMUS are available from the ARM research archive (de Boer et al. 2016a; <https://doi.org/https://doi.org/10.5439/1235273>).

Through coordination with the DOE, the DataHawk2 was operated over Oliktok Point in Restricted Area R-2204 (de Boer et al. 2016b). This airspace, extending from the surface to approximately 2 km altitude, is managed by the DOE to support UAS and tethered balloon flight activities at the site (de Boer et al. 2018). This airspace allowed for frequent profiling of the extent of the lower atmosphere. For this particular date, the DataHawk2 was primarily used in a profiling flight mode, conducting spiral ascent and descent patterns between the surface and a maximum altitude of approximately 400 m a.g.l. Most of this flight time was spent sampling a shallower layer centered on a strong inversion layer between approximately 50 and 150 m altitude.

## 2.2 Wind Measurements

Measuring wind speed and direction profiles by UAS is a more involved process than temperature, as the true winds need to be disentangled from the 3-dimensional motions of the aircraft, both of which are included in the air speed measured by the pitot tube. Motion corrections of high-frequency (e.g., 10 Hz) air speed data can be accomplished by calculating the Euler angles from the IMU and applying a rotation matrix to the raw measurements. Here, because we were not attempting to calculate fluxes, we opted for a simple and reliable estimate of wind speed using the derived aircraft heading and air speed of individual flight orbits.

In the presence of a constant horizontal wind and constant UAS air speed, the ground speed measured by the pitot tube as the aircraft completes an orbit will generally not be precisely sinusoidal, but this approximation is good when the wind speed is small relative to the airspeed (Balsley et al. 2013). The ground speed measurement is at its maximum when the UAS is oriented with a tailwind and is at its minimum when it has a headwind. For each individual orbit of the UAS a sine wave was fit (by minimizing least-squares) to the heading versus ground speed data. Wind speed was calculated as the amplitude of the sine wave, while wind direction was identified by the location of the sine wave trough. The orbits took roughly 1 min to complete and covered a mean vertical range of 40 m. To improve the spatial coverage of the resulting profiles, the calculation was done for overlapping orbits, staggered by 20° heading for each subsequent orbit. While not directly increasing the resolution, this process increased the number of measurements by 18x, creating a finer spacing through the profile. The resulting wind profiles were additionally smoothed using a locally-weighted (60% window) regression with a quadratic fit.

## 2.3 Analyses

The ABL was characterized for buoyancy and shear forces. The buoyancy term represents a resistance to buoyancy—quantified as the square of the Brunt–Väisälä frequency, or buoyancy frequency ( $N$ ):

$$N^2 = \frac{g}{\theta_v} \frac{\partial \overline{\theta_v}}{\partial z}, \quad (1)$$

where  $g$  is acceleration due to gravity,  $\theta_v$  is the absolute virtual potential temperature,  $z$  is altitude, and overbar represents a time average. This term provides a measure of the stability of fluid to displacement. The shear term is expressed as the square of the vertical shear of horizontal wind ( $S$ ) as,

$$S^2 = \left( \frac{\partial \overline{U}}{\partial z} \right)^2 + \left( \frac{\partial \overline{V}}{\partial z} \right)^2, \quad (2)$$

where  $U$  is the east–west component of the wind, and  $V$  is the north–south component of the wind. Dividing the buoyancy term by the shear term yields the gradient Richardson number ( $Ri$ ), which provides an indication of when the shear is strong enough to overcome the background stability, causing the layer to “overturn” and initiate transition between turbulent and laminar flow. Empirical studies and linear stability theory have typically identified  $\sim 0.25$  as the value below which flows become turbulent (i.e., the critical Richardson number  $[Ri_c]$ ; Taylor 1931; Miles 1961; Howard 1961; Webb 1970; Businger et al. 1971; Scotti and Corcos 1972; Rohr et al. 1988; van de Wiel et al. 2007; Ohya et al. 2008). However, stable ABLs

are often characterized by pre-existing perturbations larger than the infinitesimally small perturbations assumed by linear stability theory. Such finite amplitude instabilities shift the derived  $Ri_c$  to values higher than 0.25. Indeed, there are numerous experimental examples in which turbulence persists (sometimes well) above the typical 0.25 limit (Businger 1973; Rohr et al. 1988; Straume et al. 1998; Galperin et al. 2007; Grachev et al. 2013). Therefore,  $Ri_c$  is (to some extent) a moving target that will not precisely delineate turbulence from laminar flow. Here, for simplicity we assume that  $Ri_c$  is 0.25.

Because the data were collected as discrete points, we calculate bulk Richardson number:

$$R_B = \frac{g \Delta \bar{\theta}_v \Delta z}{\bar{\theta}_v [(\Delta \bar{U})^2 + (\Delta \bar{V})^2]}, \tag{3}$$

where  $\Delta$  represents the difference between discrete vertical layers (Stull 1988). Equations 1–3 are presented in their traditional form for mean variables, but are use here in conjunction with instantaneous profiles. Here we calculated  $R_B$  using thin, 1-m  $\Delta z$  layers. This high vertical resolution was necessary to avoid smoothing out thin intermittent turbulent layers embedded in larger stable regions. Additionally, while the typical  $Ri_c \cong 0.25$  is technically only relevant for the gradient Richardson number, it also approximates closely for  $R_B$  calculated with thin  $\Delta z$  layers (Stull 1988, p. 177).

Because  $R_B$  relies on UAS-derived  $T$ ,  $U$ , and  $V$  profiles, its use in the identification of turbulence is sensitive to any inaccuracies in the derivation of those profiles.  $T$  profiles are directly measured and are therefore expected to be highly accurate. However, because the sine fitting procedure for estimating  $(U,V)$  is applied to complete UAS orbits ( $\sim 40$  m vertical extent),  $(U,V)$  profiles are expected to smooth (to some degree) suborbital variations in wind speed. This has the potential to impact the accuracy of  $R_B$  at the fine scales we are investigating.

To confirm the validity of  $R_B$  for the stated research objectives we calculated temperature structure function parameter ( $C_T^2$ ) and turbulence kinetic energy dissipation rate ( $\epsilon$ ).  $C_T^2$  is a measure of temperature fluctuations over space, which can be used to identify atmospheric turbulence (Balsley et al. 2003, 2013, 2018; Frehlich et al. 2003; van den Kroonenberg et al. 2012; Bonin et al. 2015; Kantha et al. 2017). It was calculated from the power spectra of the high-frequency coldwire  $T$  using the formula:

$$C_T^2 = \left(\frac{2\pi}{\bar{U}}\right)^{2/3} \left[ \frac{f^{5/3} S_T(f)}{\beta} \right], \tag{4}$$

where  $S_T(f)$  is the power spectral density of  $T$  in the inertial subrange,  $f$  is frequency in Hz,  $\beta$  is the Kolmogorov constant of 0.25, and  $\bar{U}$  represents mean airspeed in  $m\ s^{-1}$  (Doddi 2021). The inertial subrange interval of  $S_T(f)$  used in fitting was centered on a frequency range of 3–10 Hz. The aircraft’s reaction to elevator commands (i.e., the system used to maintain constant airspeed) are expected to be outside this frequency range, alleviating concerns that the internal controls of the UAS influenced the  $C_T^2$  measurement.

$\epsilon$  is a measure of the wind velocity fluctuations over space. It was calculated from the power spectra of the UAS-measured airspeed using the formula:

$$\epsilon = \left(\frac{2\pi}{\bar{U}}\right) \left[ \frac{f^{5/3} S_U(f)}{\alpha} \right]^{3/2}, \tag{5}$$

where  $S_U(f)$  is the power spectral density of airspeed in the inertial subrange and  $\alpha$  is the longitudinal Kolmogorov constant of 0.52 (Lundquist and Bariteau 2015). The inertial

subrange segment used in these estimates of  $S_U(f)$  was also centered on a frequency range of 3–10 Hz. We note that  $C_T^2$  and  $\epsilon$  are proportional to each other by the dissipation rate of temperature ( $\overline{\chi}$ ; Basu et al. 2021). This measure (not calculated here) can also be used for identifying boundary layer turbulence.

The 3–10 Hz frequency range was chosen as the inertial subrange for  $\epsilon$  and  $C_T^2$  calculations because it provided the best balance of capturing small length scales of turbulence, while remaining above the instrumental noise floor. We found that both  $S_T(f)$  and  $S_U(f)$  had mean spectral slopes close to  $-5/3$  (Figs. 14 and 15), supporting the use of this inertial subrange for  $\epsilon$  and  $C_T^2$  calculations. One caveat for the use of this inertial subrange is that for the thinnest turbulent layers (e.g., 1–2 m deep), isotropic turbulence can potentially exist at length scales smaller than the 3–10 Hz range can resolve. Unfortunately, shifting the inertial subrange to higher frequencies was not possible due to the instrumental noise floor. The noise floor of the pitot airspeed measurements is high due to motor-induced vibrations at  $\sim 100$  Hz and above (see spikes in Fig. 14). The coldwire temperature measurement is inherently less sensitive to vibration, and is mounted on a vibration attenuating module. However, with both airspeed and temperature measurements, noise floors often extend to lower frequencies due to the intrinsic noise floors of the instruments, which cause a flattening of the spectral curves when the power spectral density is low. This represents a limitation of using this system for  $\epsilon$  and  $C_T^2$  calculations in very stable boundary layers. Consequently, analyses in this paper are mostly centered on the  $R_B$  measurements.

## 2.4 Case Overview

The work presented is a case study from 19 October 2016. This day represented the most strongly stable ABL measured during two collection seasons (summer/fall 2015 & 2016). The stability was the combined result of a cold surface and a clearing of the low-level stratiform clouds that are typical of the region (Fig. 2). The case study encompasses five UAS flights occurring during an 8.5-h period from 1726 UTC on 19 October 2016 to 0200 UTC on 20 October 2016 (0926–1800 local time on 19 October 2016). These flights each averaged roughly 40 min in length, for a total flight time of 3.2 h. Multiple profiles were collected during each flight. In total, 57 profiles ( $\sim 11$  per flight) were collected. The majority (45) of profiles ranged from the surface to 160 m a.g.l., while the remaining profiles (12) were flown to 400 m a.g.l. Having multiple profiles during each flight, and multiple flights over the course of the day enabled investigations into the temporal scale of processes influencing the ABL on this day.

## 2.5 Meteorological Conditions

The 10-m meteorological tower measured light SSE winds throughout the day on 19 October 2016 (Fig. 3c, d). Consequently, the DataHawk2 measured an ABL which developed over the land surface. This contrasts to the ocean fetch typically recorded at the site resulting from both the prevailing polar easterlies and seasonal westerlies.

In the days preceding the case study, radiosonde profiles showed an inversion layer developing aloft ( $\sim 1500$  m a.g.l.). It grew more prominent and descended 400–500 m each day, until it reached the surface on 19 October 2016, a day which backscatter measurements revealed was completely clear. Tower radiation measurements during the case study day showed negative net radiation during much of the day (i.e., net upwelling). Even during peak midday sun, net radiation was near zero due to negative net longwave radiation balancing

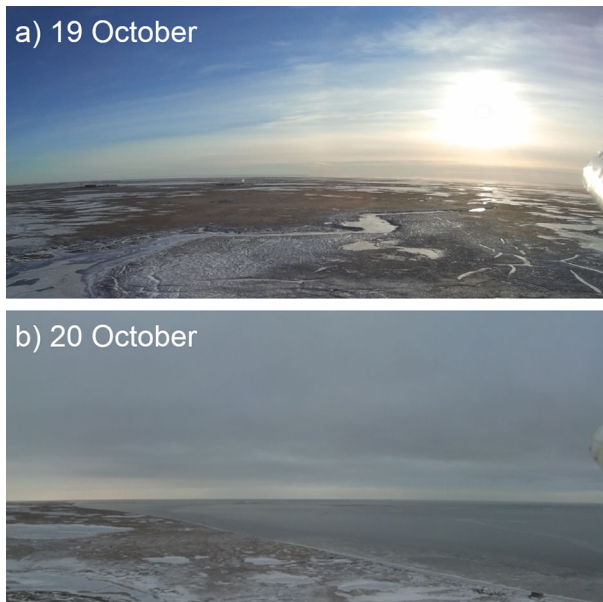


**Fig. 2** Photographs showing **a** a clear atmosphere on 19 October 2016 which resulted in the stable stratification of the lower atmosphere observed in the data presented here and **b** low-level stratiform clouds midday on 20 October 2016 (i.e., the day after the case study). The latter are more typical of the site, and generally lead to warmer near surface temperatures and less stable boundary layers

out positive net shortwave radiation (Fig. 3a). This contrasts with the more typical stratiform cloud days in which net radiation is positive during the daytime periods due to less strongly negative net longwave radiation (e.g., 18 and 20 October 2016). The radiation budget led to corresponding changes in air temperature, which dropped precipitously ( $-5$  to  $-14$  °C) throughout the night preceding the case study (Fig. 3b), setting the stage for the strongly stable ABL observed on 19 October 2016.

### 3 Results

On the morning of 19 October 2016,  $\theta$  profiles showed stable conditions throughout the 20–400 m a.g.l measurement range, with the strongest inversion located between 50 and 80 m a.g.l (Fig. 4). Here we use the height of this very strong inversion to mark the top of the SBL (the numerical identification of this height is discussed below). Above the SBL, profiles remained stable throughout the measurement range. Radiosonde data showed that this range from 80 to 400 m a.g.l was more stable than the rest of the free troposphere (FT; from  $> 600$  m a.g.l), suggesting that this region was a residual layer (RL) from an earlier SBL. The strength of stability within the measurement range weakened throughout the day, as observed by the reduced magnitude of the mean lapse rate. Deterioration of the SBL occurred from below through mechanical shear-driven turbulence. Deterioration also occurred from above—with the RL becoming more neutrally-stratified throughout the day (e.g., Flight 5 showed a neutral layer between 300 and 350 m a.g.l) and eroding the SBL capping inversion.

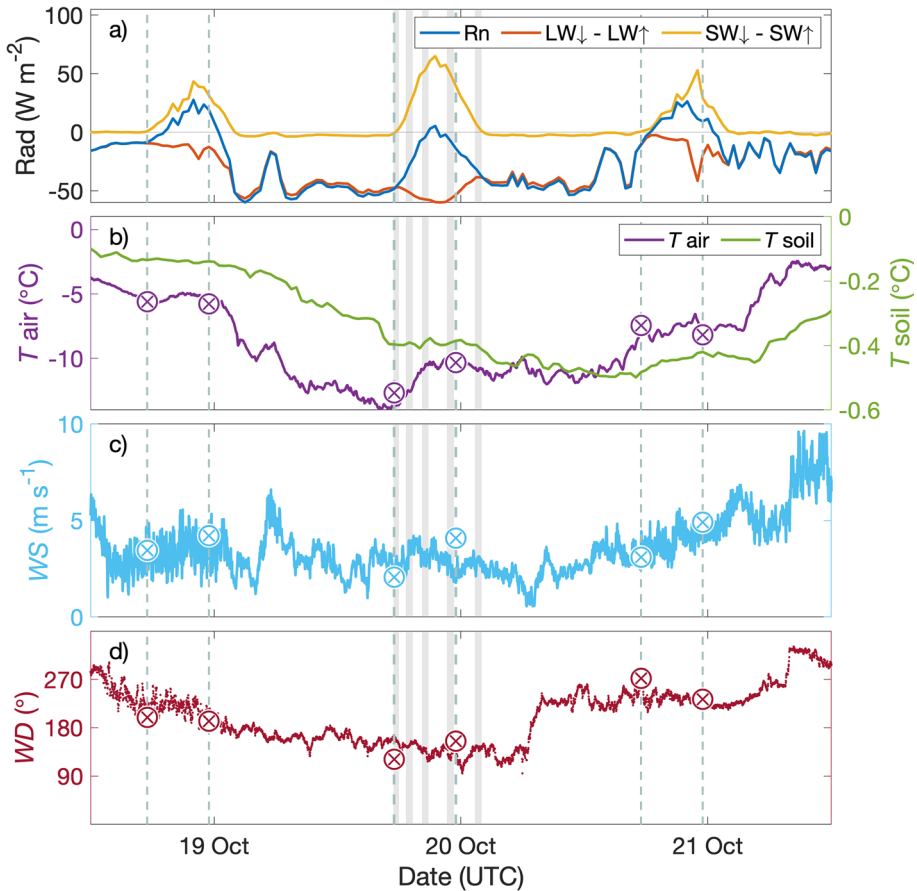


**Fig. 3** Meteorological conditions from 18 to 21 October 2016 at Oliktok Point, Alaska, showing **a** net radiation, **b** air and soil temperature, **c** wind speed, and **d** wind direction measured by the 10-m meteorological tower. The vertical gray shaded bars on 10/19 and 10/20 represent the flight times (width proportional to flight duration) from this case study. The vertical dashed lines represent times of radiosonde launches. The  $\otimes$  symbols represent the mean radiosonde measurements for **b**) air temperature, **c**) wind speed, and **d**) wind direction in the lowest 50 m a.g.l

While the flight mean  $\theta$  profiles show layers with varying degrees of stability (Fig. 4a), individual flights legs showed distinct staircase patterns in  $\theta$ , indicative of the “sheet and layer” formations found by previous studies (Dalaudier et al. 1994; Muschinski and Wode 1998; Balsley et al. 2003, 2018; Fritts et al. 2009). Figure 4b shows that the physical location of these stepped layers changed over the course of the flight. This was particularly visible from 150 to 300 m a.g.l. The synchronized radiosonde  $\theta$  profile showed the same general pattern as the DataHawk2 but had a lower vertical resolution which failed to capture the small scale of the step changes.

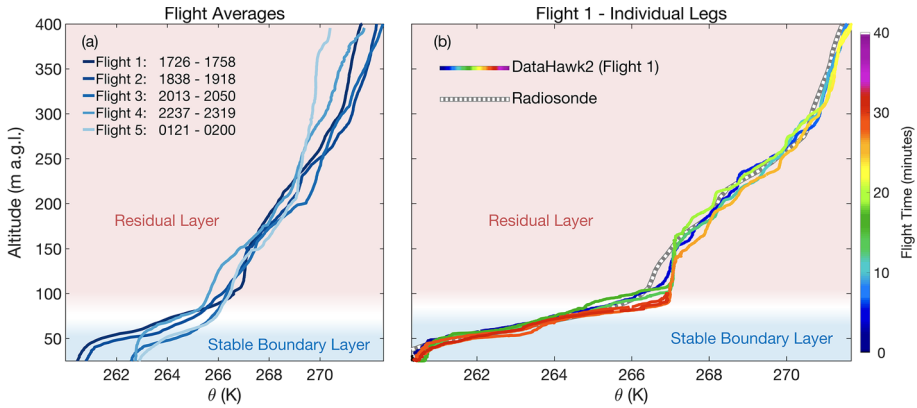


**Fig. 4 a** DataHawk2 average  $\theta$  profiles for each of the five flights and **b** DataHawk2 individual  $\theta$  profiles measured during Flight 1 (1726–1758 UTC; color represents time since takeoff) and radiosonde  $\theta$  profile (1730 UTC). The blue shaded area represents the stable boundary layer. The red shaded area represents the residual layer

### 3.1 Richardson Number

The bulk Richardson number was derived using Eq. (3) to identify regions of atmospheric turbulence. Figure 5 shows time-height cross sections of  $R_B$  throughout the lower atmosphere for each of the five case study flights. Unstable atmospheric conditions (i.e., regions with  $R_B < 0.25$ ) were observed throughout most flights from the surface to ~ 50 m a.g.l. Corresponding wind speed and  $\theta$  profiles (Fig. 5a–j) showed that for most flights this region was characterized by moderate wind shear and well-mixed conditions.

Above the surface turbulence was a persistent stable layer (the SBL) located at roughly 50–80 m a.g.l which was characterized by large increases in  $\theta$  with height ( $\sim 0.1 \text{ C m}^{-1}$ ). This represents strongly negative  $\theta$  lapse rates (defined as  $\Gamma = -d\theta/dz$ ). Wind profiles show weaker shear than the near surface environment. The median  $R_B$  for this region was 2.0 across all flights (the 25–75th percentile range was 0.6–6.3).

Above the SBL, at the bottom of the RL (from roughly 80–150 m a.g.l), the magnitude of  $\Gamma$  was much smaller (ranging from zero to slightly negative). Here the subcritical  $R_B$  layers had a more intermittent character, migrating both upwards and downward throughout the course of subsequent legs within each flight. Wind shear in this upper region was generally weak. The median  $R_B$  for this region was 0.8 across all flights, with over 25% of  $R_B$  measurements being subcritical (the 25–75th percentile range was 0.2–3.3).

Time-height cross sections of  $N^2$  (Fig. 6) show that the surface—50 m a.g.l layer is mixed with small pockets of low and high  $N^2$  (except for Flight 4 which has consistently low  $N^2$  in this layer). The strongly stable layer between 50 and 80 m a.g.l shows consistently high  $N^2$ . While the elevated layer shows large bands of intact mixed layers (identified by low  $N^2$ ) which propagate vertically, similar to the turbulent layers in the time-height cross section of  $R_B$  (Fig. 5k–o). In many instances the location of mixed layers and turbulent layers matched precisely, while in other locations mixed layers were identified as non-turbulent. The latter category occurred when mixed layers propagated into regions with wind shear too weak to maintain turbulence.

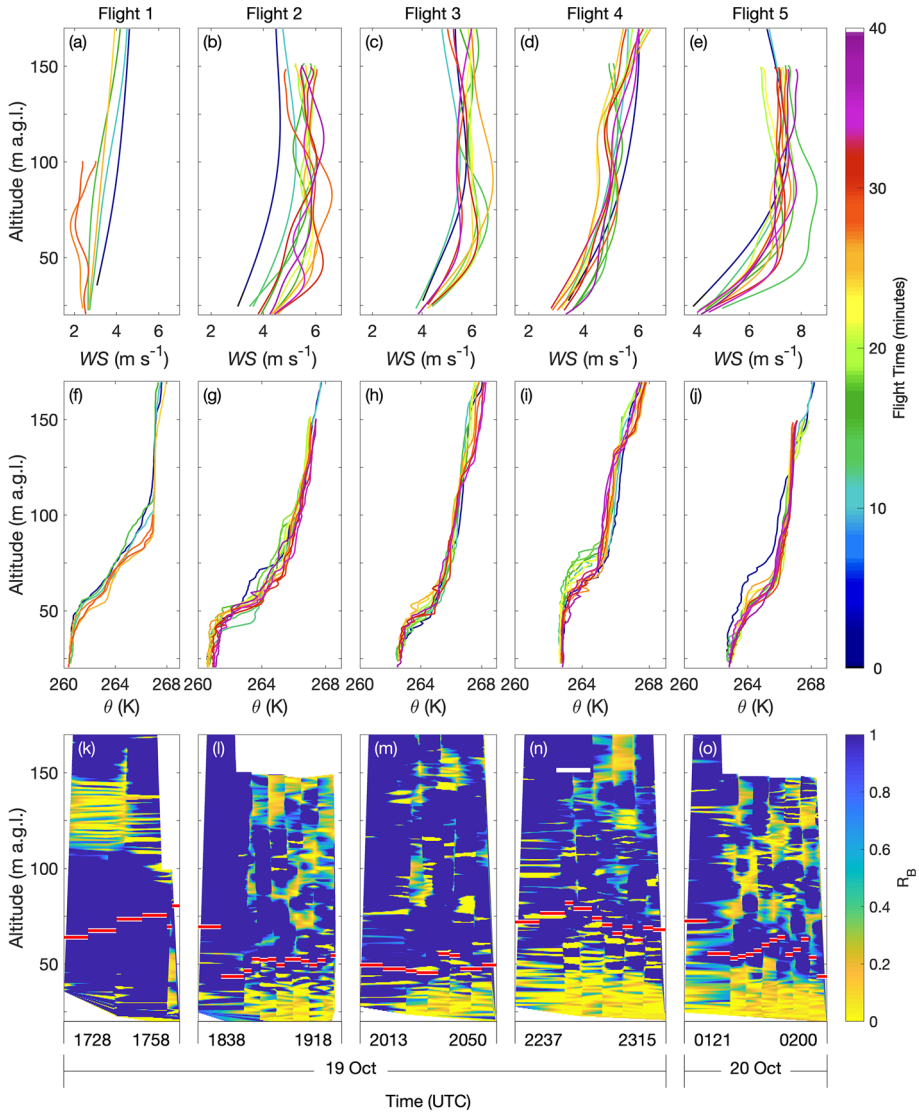


**Fig. 5** Top panels **a–e** show all wind speed profiles measured during each of the five case study flights, with color referencing flight time (in minutes from takeoff). Middle panels **f–j** show  $\theta$  profiles with the same flight time coloring as the wind speed profiles. Bottom panels **k–o** show time-height cross sections of  $R_B$ , that were interpolated between consecutive legs of each flight. Yellow regions represent turbulence (i.e.,  $R_B < 0.25$ ). The red dashes represent the height of maximum  $N^2$  ( $h_{max-N^2}$ )

### 3.2 Dissipation & Temperature Structure Function Parameter

To test the effectiveness of UAS-derived  $R_B$  for identifying atmospheric turbulence we calculated  $\epsilon$  and  $C_T^2$  from the finewire  $U$  and  $T$  datasets. During the case study, values of  $\epsilon$  ranged from  $10^{-6}$  to  $10^{-3}$  W kg<sup>-1</sup> (Fig. 8h). The correlation between  $\epsilon$  and  $R_B$  was negative

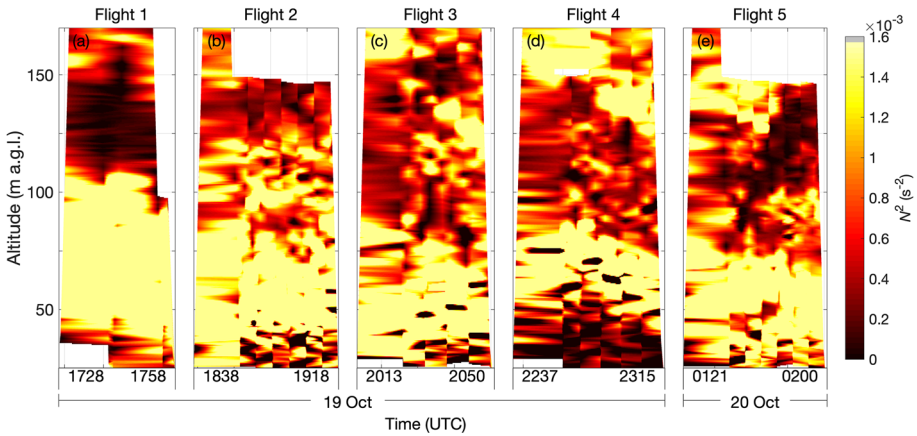


**Fig. 6** Time-height cross sections of  $N^2$ , produced by interpolating between consecutive legs of each flight. **a–e** Represent each of the five case study flights

(as expected). We found that 68% of  $R_B$ -identified “turbulence” had corresponding  $\epsilon$  values above the median  $\epsilon$  value of  $3.3e^{-5} \text{ m}^2 \text{ s}^{-3}$ .

During the case study we measured  $C_T^2$  values that ranged from  $10^{-6}$  and  $10^{-2} \text{ K}^2 \text{ m}^{-2/3}$ . While larger values of  $C_T^2$  typically indicate the presence of turbulence, there is no defined cutoff (similar to  $Ri_c$ ) for marking the transition to turbulent conditions. Additionally, it has been found that  $C_T^2$  magnitudes are larger near inversions, than in more well mixed atmospheres (Balsley et al. 2008, 2013; Bonin et al. 2015). Our data confirm previous findings regarding the strong relationship between  $d\theta/dz$  and  $C_T^2$  (Fig. 7; Basu and Holtslag 2022). What this means in a practical sense can be illustrated by comparing ABLs with constant lapse rates to those with punctuated lapse rates. In a scenario where ABL lapse rate is

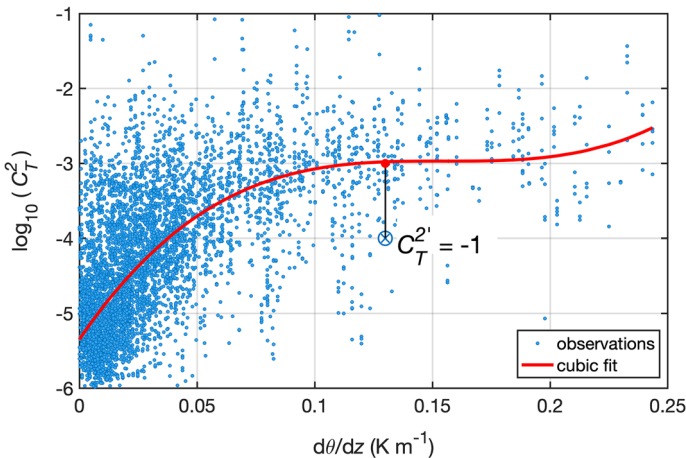


**Fig. 7** Shows  $C_T^2$  versus  $d\theta/dz$ . The red line represents the least squares cubic fit to the data.  $C_T^2$  anomaly was calculated as the deviation of each  $C_T^2$  measurement from the cubic fit. It has the same units ( $\text{K}^2 \text{ m}^{-2/3}$ ) as  $C_T^2$ , but is on a log scale—so each integer deviation represents an order of magnitude

constant, layers with larger  $C_T^2$  values have more vertical mixing (i.e., greater likelihood of turbulence). However, in an ABL punctuated with both inversions and well-mixed layers,  $C_T^2$  magnitudes are often larger near inversions (i.e., regions with lower likelihood of turbulence). This complicates the use of  $C_T^2$  as a proxy for turbulence. Indeed, we found that only 53% of  $R_B$ -identified turbulence had corresponding  $C_T^2$  values above the median  $C_T^2$  value of  $3.7e^{-5} \text{ K}^2 \text{ m}^{-2/3}$ . An example of this can be seen in Fig. 8f.

To adjust for the effects of  $d\theta/dz$  on  $C_T^2$ , we calculated a  $C_T^2$  anomaly (denoted as  $C_T^{2'}$ ).  $C_T^{2'}$  was calculated as the deviation of each  $C_T^2$  measurement from the least-squares cubic fit of the  $d\theta/dz$  vs  $C_T^2$  data (Fig. 7). The goal of this metric was to determine whether individual  $C_T^2$  measurements were high relative to other  $C_T^2$  measurements made under similar  $d\theta/dz$  conditions.  $C_T^{2'}$  profiles (Fig. 8g) were positively correlated to  $\epsilon$  (Fig. 8h), in contrast to the lack of correlation between  $C_T^2$  and  $\epsilon$ . We found that, while  $C_T^2$  values were evenly distributed above and below zero, the  $R_B$ -identified turbulent intervals had positive  $C_T^{2'}$  values 77% of the time. This shows that  $C_T^2$  measurements in turbulent layers were typically high after adjusting for the magnitude of  $d\theta/dz$ . However, 23% of measurements had negative  $C_T^{2'}$  in layers that  $R_B$  had identified as turbulent. In these cases, it was unclear whether  $C_T^{2'}$  failed as a turbulence metric or whether deficiencies in the  $R_B$  estimation falsely identified turbulence

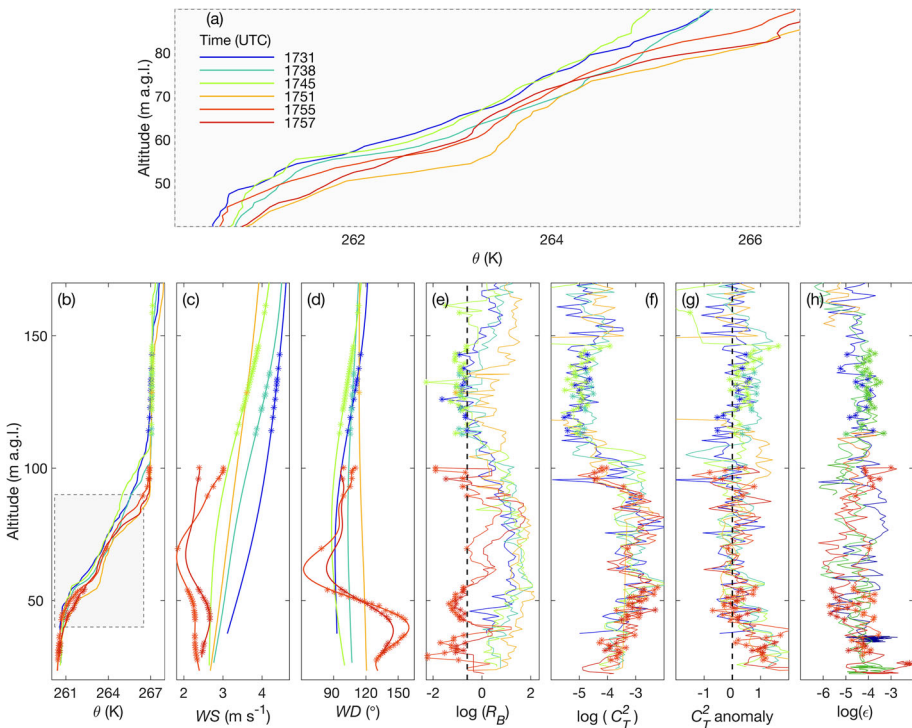


**Fig. 8** Turbulent-relevant variables measured during Flight 1 (1726–1758 UTC on 19 October 2016): **a** zoomed-in  $\theta$  (K) profile of the inset in panel **b**, **b**  $\theta$  (K), **c** wind speed ( $\text{m s}^{-1}$ ), **d** wind direction ( $^\circ$ ), **e**  $R_B$  (unitless) with vertical dashed line representing  $Ri_c = 0.25$ , **f**  $C_T^2$  ( $\text{K}^2 \text{ m}^{-2/3}$ ), **g**  $C_T^2$  anomaly, and **h**  $\epsilon$  ( $\text{m}^2 \text{ s}^{-3}$ ). Line color represents time. Star symbols in panels **b**–**h** represent measurements where  $R_B$  was below an  $Ri_c$  of 0.25 (i.e., turbulent regions)

where it did not exist. The agreement between  $C_T^{2'}$  and  $\epsilon$  suggests the latter. This supports the use of these metrics to determine whether  $R_B$ -identified turbulence is real; or at least used in conjunction with  $R_B$  to identify layers which satisfy multiple turbulence thresholds as the layers with the greatest likelihood of turbulence.

Figure 8 shows profiles of  $\theta$ , wind speed, and wind direction measured during Flight 1. At the start of this flight the layer between 50 and 90 m a.g.l was strongly stable with a consistent  $\Gamma$  of  $-0.11 \text{ C m}^{-1}$  (Fig. 8a—1731 UTC). As the flight progressed, a well-mixed layer developed in the center of the strongest part of the inversion (1738–1751 UTC), followed shortly by a return to strongly stable conditions (1755 and 1757 UTC). The development of this mixed layer within such a strongly stable layer provides an opportunity to examine the causes of intermittent turbulences. Previous research suggests that turbulent layers can propagate downwards or upwards (Sun et al. 2004; Sullivan et al. 2016). However, in this instance there was no observable turbulent layer propagating into the region from above or below. Additionally, the  $U$  profiles leading up to its formation show very little shear with which to initiate turbulence. The strong stability or lack of shear forces needed to generate turbulence suggests that the mixed layer was advected into the study area.

The most notable feature surrounding this event was that the development of the well mixed layer preceded (by a few minutes) a substantial wind speed drop and wind direction shift. The reduced wind speed that followed in the wake of the mixed layer allowed an existing wind direction shear (mean difference of  $65^\circ$  for Flight 1) between southerly surface winds (measured on the 10-m EC tower) and easterly winds just above the surface (measured by the UAS) to ascend to 50 m a.g.l. Notably, a nearly identical wind directional shear was measured by the radiosonde 25 min earlier (1730 UTC). However, the nearly synchronous UAS leg (1731 UTC) did not show a wind directional shear. This suggests that such upward progressions of directional shear are either short-lived or have short lateral extents (as the radiosonde immediately moved away from the release point near the UAS profiling location). Such small scale (whether spatial or temporal) is also evidenced by the mixed layer observed in Fig. 8 beginning to disappear only minutes after it arrived/formed.

### 3.3 Turbulent Layer Characteristics

The characteristics of turbulent layers were investigated by measuring the physical dimensions of subcritical layers identified by the  $R_B$  analysis. These layers were identified as  $R_B < Ri_c \equiv 0.25$  using the 1-m resolution  $R_B$  measurements. It was found that over half of all individual, noncontiguous layers were 1 m or less deep (Fig. 9). Weighting the frequency of occurrence of turbulence with layer depth ( $fd / \sum_{d=1}^{\infty} fd$ , where  $f$  is frequency and  $d$  is layer depth), it was found that half of all turbulence was occurring in individual layers less than 4 m deep. Applying smoothing to the  $\theta$  profiles prior to calculating  $R_B$  necessarily increased the frequency and overall contribution of thicker layers to total turbulence, but distribution of turbulence always clustered around the smallest unit of measurement. Additionally, because of the smoothing inherent in the wind estimation, the peak of the distribution of turbulent layer thickness is likely even smaller than measured here.

The vertical propagation of layers in the lower atmosphere was assessed by measuring the change in altitude of the SBL top during successive profiles. The SBL top can be identified in multiple ways. One common method is to equate it to the altitude of the largest temperature gradient, i.e., the strongest part of the capping inversion (Beyrich 1997; Hyun et al. 2005; Balsley et al. 2006; Hennemuth and Lammert 2006; Martucci et al. 2007). To identify that we followed the method of Balsley et al. (2006) and found the height of maximum  $N^2$  ( $h_{max-N^2}$ ;

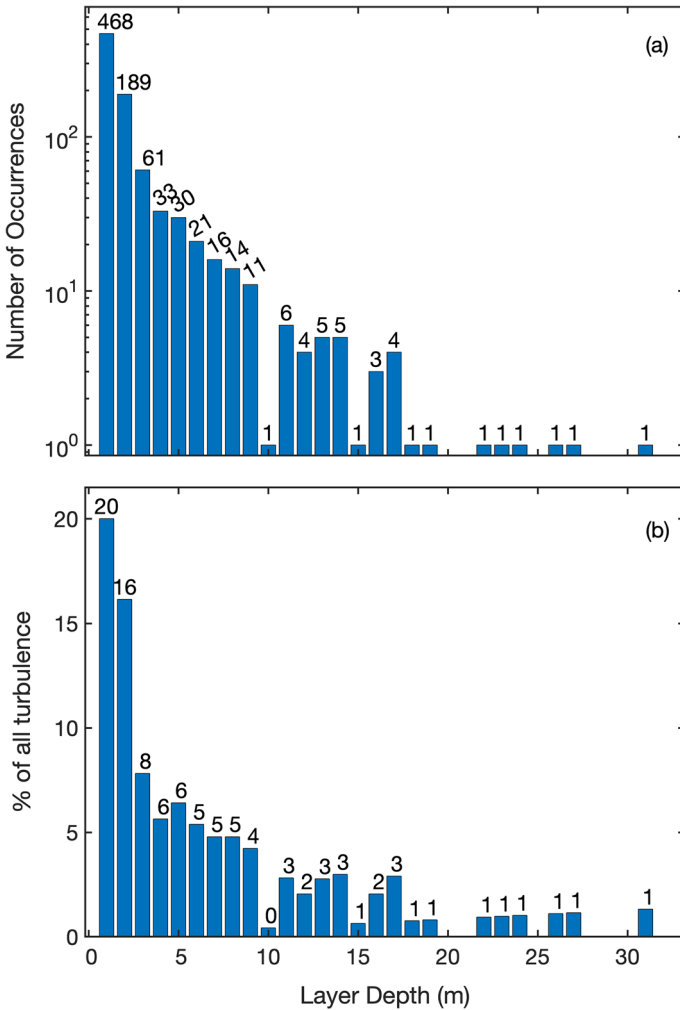


**Fig. 9** **a** Frequency of discrete turbulent layers (i.e., discontinuous with other turbulent layers) of different depths. **b** Distribution of total percentage of turbulence of different layer depths (i.e., a weighted distribution:  $fd / \sum_{d=1}^{\infty} fd$ , where  $f$  is frequency and  $d$  is layer depth)

shown in Fig. 5k–o).  $h_{max-N^2}$  was identified for each flight leg as the median height of the top 5% of the measured  $N^2$  values. The vertical propagation velocity associated with the SBL top was determined by finding the difference in  $h_{max-N^2}$  between subsequent legs and dividing it by the time difference between those legs. The distribution of vertical propagation velocities was centered on zero, with 80% of the measurements exhibiting propagation velocities within  $-4.5$  to  $+3.3$   $\text{cm s}^{-1}$  (Fig. 10). The largest magnitude vertical propagation velocity between consecutive legs was  $10$   $\text{cm s}^{-1}$ , while the median was  $1.7$   $\text{cm s}^{-1}$ .

The meteorological dataset was investigated for correlations with  $h_{max-N^2}$ . Wind speed and  $h_{max-N^2}$  were inversely correlated on longer (multi-hour) timescales (Fig. 11), so that when wind speed increased  $h_{max-N^2}$  moved towards the surface. Interestingly, on shorter time

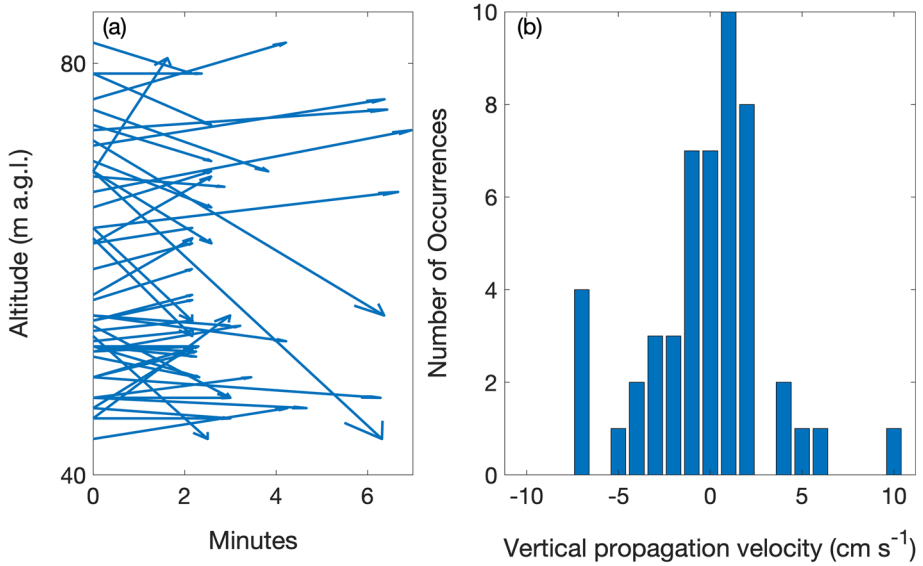


**Fig. 10** Shows **a** vectors of vertical propagation derived from the ABL height analysis and **b** the distribution of vertical propagation velocity

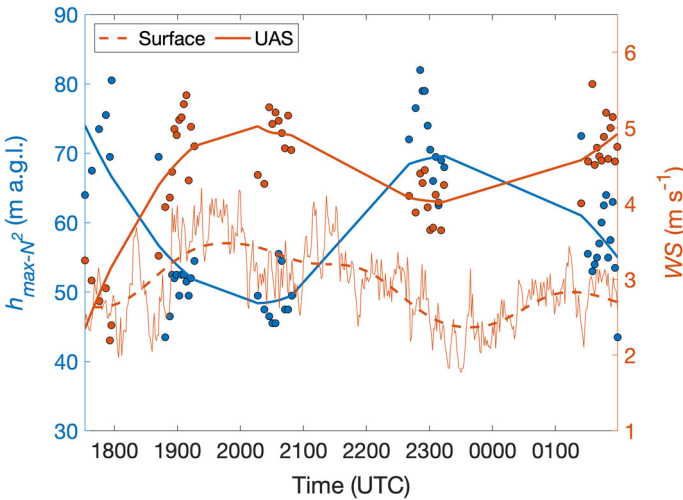


**Fig. 11** Wind speed (UAV and surface) and  $h_{max-N^2}$  over the course of all five flights on 19 October 2016. Dots represent UAV mean values for each flight leg

scales the negative wind speed and  $h_{max-N^2}$  relationship breaks down, and even potentially becomes positive. This can be seen in the tracking between wind speed and  $h_{max-N^2}$  that frequently occurs in Fig. 12.

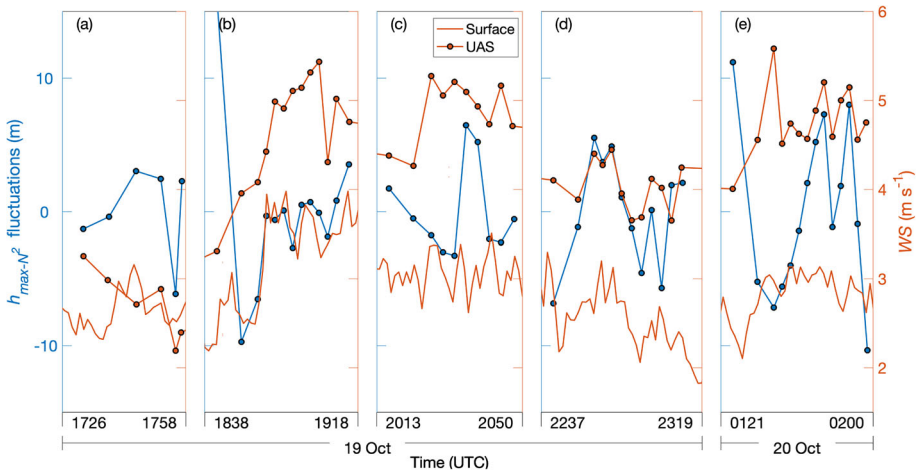


**Fig. 12** Shows the same information as Fig. 11, but with two modifications to show within flight variations more clearly: (1.) individual panels (a–e) for each flight to widen the representation of the flight times on the figure and (2.)  $h_{max-N^2}$  shown as fluctuations rather than actual values to prevent the larger, long-term variations from minimizing the ability to see shorter, small-scale variations

## 4 Discussion

The strong stability observed on 19 October 2016 at Oliktok Point was the result of radiative cooling arising from cloud-free conditions, which reduced the longwave surface warming typically introduced by a persistent low-level stratiform cloud layer. Throughout the entire measurement range (20–400 m a.g.l) the atmosphere had stable thermal stratification. For all flights the height of strongest inversion was roughly 50–80 m above the surface. While conventions vary, we named the region below the strong inversion the stable boundary layer (SBL) and the weakly stable region above it, but below the free troposphere, the residual layer (RL). Intermittent turbulence was observed throughout all flights in both the SBL and RL, and occasionally even within the inversion layer separating the two. The characteristic staircase pattern in  $\theta$  found by previous studies was observed (Daludier et al. 1994; Muschinski and Wode 1998; Balsley et al. 2003, 2018; Fritts et al. 2009; Sullivan et al. 2016). Similarly, the staircase pattern was found to be vertically mobile, shifting upwards and downwards.

Within a thermally stratified layer shear forces create turbulence, while buoyancy forces and viscous dissipation destroy turbulence (Steenefeld 2012). While shear in SBLs is the *cause* of turbulence, both shear and buoyancy forces influence whether it materializes. It is useful to identify the balance of those forces when characterizing the nature of turbulence within the SBL.  $R_B$  is effectively a ratio of buoyancy resistance ( $N^2$ ) to wind shear ( $S^2$ ). Therefore, low  $R_B$  values (i.e., turbulent conditions) arise when the numerator  $N^2$  is small or the denominator  $S^2$  is large (or both). Identifying which of those conditions is responsible for low  $R_B$  can help identify the causes of turbulence within the different layers.

The data in this study show that turbulence is both shear and buoyancy driven. Within the SBL (i.e., the area below  $h_{max-N^2}$ ), turbulence was typically generated by wind shear. This was illustrated by the time-height cross section of  $N^2$  (Fig. 6). Higher  $N^2$  is often found in the lowest 80 m a.g.l (Fig. 6a, b, c, e; exception Fig. 6d). This means that there is a large increase in  $\theta$  with height in these layers. When such layers are not stable it is due to shear

forces. These were observed as directional shear (strongest in the morning) and wind speed shear (strongest later in the day). Directional shear was indicated by a difference between wind direction of the lowest UAS measurements and those of the 10-m tower. With the calm winds on this day and the strong stability decoupling the surface from the winds aloft, it is likely that the southerly surface wind direction represented either a drainage flow or a land breeze. The altitudinal interface of this directional shear was generally confined below 20 m, but it rose higher when ambient wind speed weakened, as seen on the final legs of Flight 1 (Fig. 8). While the magnitude of the directional difference was largest ( $65^\circ$ ) during Flight 1, it persisted at a mean of  $20^\circ$  throughout the rest of the day and was partially responsible for generating shear below the inversion. Such directional shear within thin (10 m) surface layers was also found by Sun et al. (2004). In the afternoon, the weaker directional shear was accompanied by strong wind speed shear at the surface. This was observed in the wind speed profiles in Fig. 5a–e. Such shear-driven turbulence near the surface is typical, due to friction with the surface and surface features (Durst 1933; Allouche et al. 2022). Due to the constant source of shear, these layers of the SBL near the surface had relatively continuous turbulence throughout the day, compared to the RL above the inversion.

In the RL, turbulence was more influenced by buoyancy. In this region  $N^2$  (Fig. 6) was lower than in the SBL, meaning  $\Gamma$  was much smaller. The more well-mixed nature of these layers means they had greater likelihood of turbulence, as they didn't require strong wind shear to overcome resistance to turbulence observed in layers with more strongly negative  $\Gamma$ . Similar to previous SBL studies (Blackadar 1957; Balsley et al. 2003, 2006; Sun et al. 2004; Sullivan et al. 2016), this study showed a weak LLJ during most profiles. It was located right at the bottom of the RL—on average  $31 \pm 21$  m above  $h_{max-N^2}$ . This matches strikingly well with the findings of Balsley et al. (2006). At its peak, the LLJ represents (in theory) the height of minimum shear; because the wind speed is relatively constant. In this study, shear profiles (not shown) had multiple locations of minimum shear, due to multiple peaks and troughs in the wind speed profiles, and degrees of directional shear that extended throughout the profiles. At such locations conditions were seldom turbulent. However, distributed throughout the RL were regions of moderate shear that overlapped with the lower values of  $N^2$ . At these locations, the  $R_B$  analysis identified turbulence. However, because the LLJ proved a weaker and more variable source of turbulence than the surface, the turbulence in the RL was more intermittent and migratory than in the SBL (Fig. 5k–o).

Episodes of well-mixed layers were even found to materialize in the middle of the extremely stable inversion layer. The before and after  $\theta$  profiles of the example discussed in Sect. 3.2 (Fig. 8a) showed similarity with the simulated  $\theta$  profiles of Fritts et al. (2003; their Fig. 3) which showed the temporal development through and between turbulent billows. They showed the decay of turbulence occurred in roughly 4 min—a comparable timescale to our event. However, upon inspection, the Richardson number during this episode stayed within the stable regime (Fig. 5k), due to the lack of accompanying wind shear. Therefore, this episode appears to be an example of a residual mixed layer from recently decayed turbulence which advected into the study area from an upwind location (Nakamura and Mahrt 2005). Our results support the Arctic SBL multi-level tower measurements of Allouche et al. (2022), who found that close to the surface shear forces were largely responsible for generating turbulence, while at higher measurement levels intermittent turbulent bursts were advected by mean flow and/or lofted from lower levels by turbulent ejections.

The partial disconnect between the location of well-mixed layers and turbulent layers (like the previous example) was observed throughout the measurement range, identifiable by the differences in the  $N^2$  and  $R_B$  time-height cross sections (Figs. 5k–o and 6a–e). It reveals that the processes generating and suppressing turbulence are occurring simultaneously within our

study domain. Small-scale pockets of turbulence form where buoyancy and shear forces are of appropriate magnitude, while turbulence decays where one or both of those forces cannot sustain turbulence. This is in line with previous finding that active, decaying, and fossil turbulence occur on small temporal and spatial ( $< 1$  m) scales within SBLs (Muschinski and Wode 1998; Balsley et al. 2003, 2006; Nakamura and Mahrt 2005).

As discussed above, with the present dataset it seems likely that a weak drainage flow below and a LLJ above the inversion were at least partially responsible for generating the shear required overcome the resistance buoyancy caused by the thermal stratification. It is possible that other phenomena documented to initiate turbulence in SBLs (e.g., gravity waves, density currents, sub-mesoscale motions) were present, but the nature of the UAS dataset precludes their identification.

A key characteristic of intermittent turbulence in this (and previous [e.g., Allouche et al. 2022]) SBL studies was vertical propagation. Here we measured the vertical propagation of  $h_{max-N^2}$  as an indication of the rate of changed in altitude of layers in the lower atmosphere. This was not a direct measure of the vertical propagation velocity of *turbulent* layers, as the region of maximum  $N^2$  represents the *most* stable altitudes in the profile. However, the vertical movement of inversions has been used previously to document vertical propagation in SBLs, due to their easy identification (Balsley et al. 2003, 2006; Sullivan et al. 2016). The challenge with applying a similar analysis directly to turbulent layers is that the identification of temporally-continuous turbulent layers in the time-height cross sections is more subjective. Fortunately, the propagation of both turbulent layers in Fig. 5 and mixed layers in Fig. 6 often appeared to track with  $h_{max-N^2}$ , suggesting that the vertical propagation of turbulence is closely tied to the broader changes in vertical structure within the ABL.

Here we found the median magnitude of vertical propagation velocity to be  $1.7 \text{ cm s}^{-1}$ . Interestingly, when compared to propagation velocities measured by previous studies a scale dependence becomes evident (Fig. 13). The LES results of Sullivan et al. (2016) showed propagation velocities of  $100\text{--}200 \text{ cm s}^{-1}$  between measurement intervals of 1.5 s. Using a tethered lifting system during the CASES-99 field campaign, Balsley et al. (2003) found a vertical propagation velocity of  $-16 \text{ cm s}^{-1}$  over a 45 s period. Our value of  $1.7 \text{ cm s}^{-1}$  was calculated between flight legs an average of 3 min apart. In a broader investigation into ABL height shifting over several different days Balsley et al. (2006) showed median vertical propagation velocities of  $0.5 \text{ cm s}^{-1}$  between periods with a mean of 45 min. For a further check, we recalculated the propagation velocities from our study using flight mean  $h_{max-N^2}$  altitude changes, instead of individual legs (i.e., the blue line in Fig. 11 instead of Fig. 12). Even though the actual magnitude of the elevation change is much larger between flight means than individual flight legs, the longer time scales result in the propagation velocities (i.e.,  $\Delta \text{ height} / \Delta \text{ time}$ ) being smaller in magnitude. Using this approach, the median vertical propagation velocity dropped to  $0.25 \text{ cm s}^{-1}$  for flights an average of 2 h apart. This shows that small-scale turbulence is capable of propagating vertically faster than large-scale, but that such short-term variability doesn't necessarily translate to a change of atmospheric state over the longer term, a finding consistent with Balsley et al. (2003). That the SBL remains relatively constant over 9 h (with  $\sim 5 \text{ m s}^{-1}$  winds) indicates that the lateral extent of the inversion layer is at least  $100\text{--}200 \text{ km}$ . This persistent layer appears to constrain the boundaries of shorter-term variability.

Balsley et al. (2003) note that vertical propagation of coherent structures can be the result of either true vertical velocities in the atmosphere or the advection of a tilted layer as it moves past the sensor. The latter explanation is similar to that offered by Sullivan et al. (2016)—that vortical structures that arise on both sides of tilted temperature fronts. Combining our measured vertical propagation velocities for  $h_{max-N^2}$  with corresponding

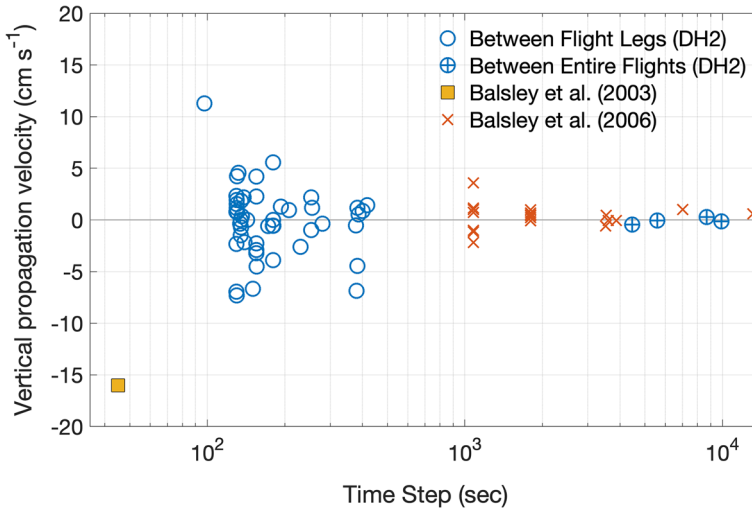


**Fig. 13** Vertical propagation velocity versus the time increment between measurements. Blue circles represent the propagation velocities between DataHawk2 flight legs shown in Fig. 10. Blue circles with pluses represent the same dataset, but with propagation velocity calculated between flight mean  $h_{max-N^2}$  altitude changes instead of individual legs. Balsley et al. (2003, 2006) values are also included. Relevant, but omitted for plot display reasons, is Sullivan et al. (2016) whose LES results showed propagation velocities on the order of  $100 \text{ cm s}^{-1}$  at short timescale of 1.5 s

wind speeds we estimate that, if vertical propagation were the result of tilt, the tilt angles would average  $\pm 0.3^\circ$ . This is less than the  $1^\circ$  tilt estimated by Balsley et al. (2003). It is almost two orders of magnitude less than the  $\sim 15^\circ$  tilt shown in LES model results of Sullivan et al. (2016). These tilt differences show the same scale relationship as the propagation velocities.

The vertical propagation of layers within the SBL is clear. However, whether its vertical velocity or tilted layers, the cause of those conditions remains less clear. Our data show a correlation between vertical propagation of  $h_{max-N^2}$  and horizontal wind speed. Over hourly timescales there is a clear inverse relationship (Fig. 11). Because causality cannot be determined, it is unclear whether  $U$  forces SBL height or SBL height forces  $U$ . If the former, a potential explanation is that when  $U$  increases, turbulence above the inversion increases. The downward momentum of turbulence subsequently forces a downward movement of  $h_{max-N^2}$ . If the latter, when SBL height increases,  $U$  decreases due to more volume for the same pressure forcing.

Over shorter timescales the inverse relationship breaks down (Fig. 12). The frequent tracking between  $U$  and SBL height even suggests the possibility of a positive relationship. One potential explanation for this difference, is that at small scales the influence of individual eddies may be able to directly force changes in SBL height. For example, a small downward gust from the residual layer may be able to temporarily decrease  $h_{max-N^2}$ , which the persistent landscape-wide SBL will return to its original height over longer timescales.

An unrelated explanation for the varying height of  $h_{max-N^2}$  over longer timescales is the passage of mesoscale motions. Low frequency disturbances can be caused by a variety of atmospheric phenomena (e.g., gravity waves, density currents, Kelvin–Helmholtz instabilities, etc.), which have been found to influence vertical structure and transport within SBLs (Fritts et al. 2003; Mahrt and Vickers 2003). Additionally, studies have shown that  $\theta$  profiles vary spatially under heterogeneous surface conditions (Mahrt 1987; Medeiros and Fitzjarrald

2014). Such surface heterogeneity can result in the formation of sub-mesoscale eddies (Eder et al. 2015). Because this study area was composed of a mix of freezing lakes, rivers, and tundra, characteristic of much of the coastal region on the North Slope of Alaska (Fig. 1), it is possible that the differential surface heating resulted in the formation of sub-mesoscale motions. If so, these may be implicated in the slight wind direction meandering throughout the day, and potentially a source of changes to  $h_{max-N^2}$ . Unfortunately, the scope of the dataset precludes carrying out a robust investigation into the influence of mesoscale processes.

Models need empirical corrections for mixing in SBLs in order to ameliorate the current biases (Tjernström et al. 2005; Cuxart et al. 2006; Steeneveld 2014). Unfortunately, observational and theoretical support for such corrections is limited (Medeiros and Fitzjarrald 2014). UAS measurements provide an avenue to collect repeated high-resolution profiles. Here we show that UAS can be used to identify turbulence within fine resolution layers and observe their vertical propagation. While  $R_B$  is not a direct measure of turbulence, the bulk of empirical studies support the use of critical Richardson number of 0.25 for identifying turbulence (Medeiros and Fitzjarrald 2014). The use of  $C_T^2$  and  $\epsilon$  provided additional measures of mixing unrelated to  $R_B$ . While the interpretation of  $C_T^2$  can be challenging in ABLs with punctuated  $\theta$  profiles (Balsley et al. 2008, 2013; Bonin et al. 2015), we show that the  $C_T^2$  anomaly (i.e., deviation from  $C_T^2$  vs.  $d\theta/dz$  relationship) results in a similar turbulent structure to that of  $R_B$ . This suggests that the anomaly may be useful for improving interpretability of  $C_T^2$  in SBLs. However, one aspect that limited the current dataset was the lack of high-frequency vertical velocity measurements. Future studies attempting to use UAS for developing sub-grid parameterizations for SBLs in NWP, should consider deploying flux packages capable of providing high frequency observations of atmospheric vertical motion. These measurements would allow for the direct identification of turbulence (as in the present study), but would also provide the ability to assess flux divergence profiles of heat and momentum. Flux measurements would also enable the direct derivation of gradient-based similarity scaling relationships for stable layers decoupled from the surface (Sorbján and Grachev 2010), and allow for field testing the accuracy of short vs long-tailed stability functions.

Fortunately, much work has been done since this campaign to create, test, and deploy small flux measurement systems for UAS (e.g., Cleary et al. 2022; de Boer et al. 2022; Nuijens et al. 2022; Tirado et al. 2023). Momentum and sensible heat fluxes measured by UAS were found to agree well with colocated tower eddy covariance measurements (de Boer et al. 2023). This highlights the future potential of such platforms to investigate the dynamics of stable boundary layers. One such application for UAS with flux payloads could be to test modeled and analytic solutions. One example being the analytical results of Basu and Holtslag (2022), which showed that the ratio of  $C_T^2$  to  $(d\theta/dz)^2$  was related to a length scale with a possible application as a proxy for turbulence. The ability to obtain in-situ measurements of momentum flux would facilitate further investigation of such analytical solutions.

## 5 Conclusions

Observational data are necessary to develop a more fundamental understanding of the SBL and the nature of the coherent structures embedded within them. Such measurements are necessary for improving NWP model parameterizations of subgrid turbulence. Here we used a UAS platform to investigate intermittent turbulence in a very stable boundary layer over a coastal plane on the North Slope of Alaska. We derived  $R_B$ ,  $\epsilon$ , and  $C_T^2$  from the UAS data to characterize the dimensions and propagation of turbulent layers. The lower atmosphere in

this environment was characterized by a SBL in the lowest 80 m a.g.l with an RL above. In the different regions of the profile, turbulence was driven by a different balance of buoyancy and shear forces, with turbulence in the near surface SBL driven by strong shear forces overcoming strong resistance to buoyancy, while turbulence in the RL characterized by weaker shear forces from a LLJ overcoming weaker resistance to buoyancy.

The  $R_B$  analysis showed distinct turbulent layers ranging from 1 to 30 m deep, both above and below a strong near-surface inversion. Most individual layers were 1–2 m deep and appeared to travel both upwards and downwards across successive flight legs. Vertical propagation velocity of the lower atmosphere was assessed by measuring the rate of change in height of the strong inversion, which appeared to track well with the vertical movements of the mixed layers above and below. Propagation velocities ranged from  $-4.50$  to  $+3.25$  cm s<sup>-1</sup>, with a median velocity magnitude of 1.7 cm s<sup>-1</sup>. Such propagation velocities were timescale dependent, with larger velocities at small scales and lower velocities when averaging over longer timescales. This suggests that the underlying conditions generating the SBL had a large spatial extent and likely moderated deviations in height caused by smaller-scale variability.

The analyses conducted in this study also confirmed previous findings that intermittent turbulence can be active or decaying. This was apparent in the imperfect overlap between locations of turbulence identified by  $R_B$  and mixed layers identified by  $N^2$ . Such instances show that some mixed layers are remnants of previous turbulence that advected past the measurement column. This was specifically observed in the passage of a mixed layer through the strongest part of the inversion during Flight 1.

While identifying the precise causes of turbulence remains challenging, we show that the unique abilities of UAS platforms (e.g., their high temporal resolution and ability to collect repeat profiles on the order of minutes) afford some advantages for investigating small-scale processes in SBLs. Future UAS deployments with flux packages are a promising route for further investigations.

**Acknowledgements** We would like to thank the Oliktok Point site technicians and the pilots, engineers, and research staff of the University of Colorado's Integrated Remote and In Situ Sensing Program (IRISS) for their efforts in collecting the datasets presented here. We would also like to thank the three anonymous reviewers for their constructive reviews of this manuscript.

**Author Contributions** BB wrote the main manuscript text and prepared the figures. GdB and DL developed the UAS, planned the field experiment, deployed the UAS in the field, and provided feedback on the manuscript.

**Funding** This work was supported by the U.S. Department of Energy (DOE), the National Oceanic and Atmospheric Administration (NOAA), and the National Science Foundation (NSF). This includes support through grants (DOE Office of Science Project Numbers DE-SC0011459, DE-SC0013306) and through direct funding by the NOAA Physical Sciences Laboratory. Additional direct funding was provided by Pacific Northwest National Laboratories and Sandia National Laboratories for DataHawk2 deployment and operations. Development of the DataHawk2 vehicle and sensors was funded in part by the National Science Foundation under grant AGS-1041963. The DOE Atmospheric Radiation Measurement (ARM) Program supported site operations at Oliktok Point.

**Data Availability** The data presented in this manuscript are available online on the ARM Data Discovery repository. Accessible at: <https://www.arm.gov/data/>

## Declarations

**Competing interests** The authors declare no competing interests.

**Open Access** This article is licensed under a Creative Commons Attribution 4.0 International License, which permits use, sharing, adaptation, distribution and reproduction in any medium or format, as long as you give

appropriate credit to the original author(s) and the source, provide a link to the Creative Commons licence, and indicate if changes were made. The images or other third party material in this article are included in the article's Creative Commons licence, unless indicated otherwise in a credit line to the material. If material is not included in the article's Creative Commons licence and your intended use is not permitted by statutory regulation or exceeds the permitted use, you will need to obtain permission directly from the copyright holder. To view a copy of this licence, visit <http://creativecommons.org/licenses/by/4.0/>.

## Appendix

See Figs. 14 and 15.

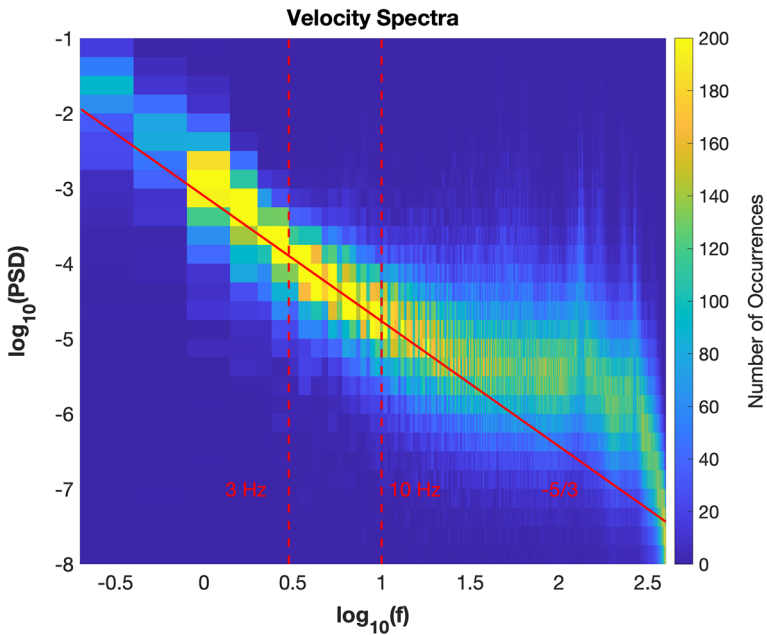


**Fig. 14** Surface plot showing the power spectra for the velocity measurements used in the calculation of  $\varepsilon$ . The color represents density of the all spectra measured during Flight 1 (note: the other flights show the same behavior). Within the range of 3–10 Hz we found that there was convergence of the spectral slopes from all flux intervals to a mean of roughly  $-5/3$

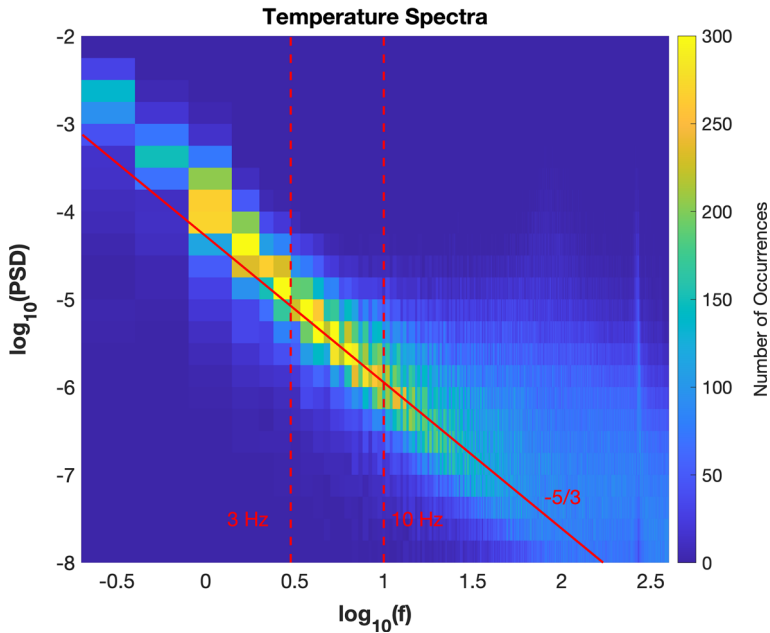


**Fig. 15** Surface plot showing the power spectra for the temperature measurements used in the calculation of  $C_T^2$ . The color represents density of all spectra measured during Flight 1 (note: the other flights show the same behavior). Within the range of 3–10 Hz we found that there was convergence of the spectral slopes from all flux intervals to a mean of roughly  $-5/3$

## References

- Allouche M, Bou-Zeid E, Anson C et al (2022) The detection, genesis, and modeling of turbulence intermittency in the stable atmospheric surface layer. *J Atmos Sci* 79:1171–1190. <https://doi.org/10.1175/JAS-D-21-0053.1>
- Balsley BB, Frehlich RG, Jensen ML et al (2003) Extreme gradients in the nocturnal boundary layer: structure, evolution, and potential causes. *J Atmos Sci* 60:2496–2508. [https://doi.org/10.1175/1520-0469\(2003\)060%3c2496:EGITNB%3e2.0.CO;2](https://doi.org/10.1175/1520-0469(2003)060%3c2496:EGITNB%3e2.0.CO;2)
- Balsley BB, Frehlich RG, Jensen ML, Meillier Y (2006) High-resolution in situ profiling through the stable boundary layer: examination of the SBL top in terms of minimum shear, maximum stratification, and turbulence decrease. *J Atmos Sci* 63:1291–1307. <https://doi.org/10.1175/JAS3671.1>
- Balsley BB, Svensson G, Tjernström M (2008) On the scale-dependence of the gradient Richardson number in the residual layer. *Boundary-Layer Meteorol* 127:57–72. <https://doi.org/10.1007/s10546-007-9251-0>
- Balsley BB, Lawrence DA, Woodman RF, Fritts DC (2013) Fine-scale characteristics of temperature, wind, and turbulence in the lower atmosphere (0–1300 m) over the south Peruvian coast. *Boundary-Layer Meteorol* 147:165–178. <https://doi.org/10.1007/s10546-012-9774-x>
- Balsley BB, Lawrence DA, Fritts DC et al (2018) Fine structure, instabilities, and turbulence in the lower atmosphere: high-resolution in situ slant-path measurements with the DataHawk UAV and comparisons with numerical modeling. *J Atmos Ocean Technol* 35:619–642. <https://doi.org/10.1175/JTECH-D-16-0037.1>
- Banta RM, Mahrt L, Vickers D et al (2007) The very stable boundary layer on nights with weak low-level jets. *J Atmos Sci* 64:3068–3090. <https://doi.org/10.1175/JAS4002.1>
- Basu S, Holtslag AA (2022) Revisiting and revising Tatarskii's formulation for the temperature structure parameter (CT 2) in atmospheric flows. *Environ Fluid Mech* 22:1107–1119
- Basu S, DeMarco AW, He P (2021) On the dissipation rate of temperature fluctuations in stably stratified flows. *Environ Fluid Mech* 21:63–82. <https://doi.org/10.1007/s10652-020-09761-7>

- Beyrich F (1997) Mixing height estimation from sodar data: a critical discussion. *Atmos Environ* 31:3941–3953. [https://doi.org/10.1016/S1352-2310\(97\)00231-8](https://doi.org/10.1016/S1352-2310(97)00231-8)
- Blackadar AK (1957) Boundary layer wind maxima and their significance for the growth of nocturnal inversions. *Bull Am Meteorol Soc* 38:283–290. <https://doi.org/10.1175/1520-0477-38.5.283>
- Bonin TA, Goines DC, Scott AK et al (2015) Measurements of the temperature structure-function parameters with a small unmanned aerial system compared with a sodar. *Boundary-Layer Meteorol* 155:417–434. <https://doi.org/10.1007/s10546-015-0009-9>
- Businger JA (1973) Turbulence transfer in the atmospheric surface layer. In: Haugen DA (ed) Workshop on micrometeorology. AMS, Boston
- Businger JA, Wyngaard JC, Izumi Y, Bradley EF (1971) Flux-profile relationships in the atmospheric surface layer. *J Atmos Sci* 28:181–189. [https://doi.org/10.1175/1520-0469\(1971\)028%3c0181:FPRITA%3e2.0.CO;2](https://doi.org/10.1175/1520-0469(1971)028%3c0181:FPRITA%3e2.0.CO;2)
- Cleary PA, de Boer G, Hupy JP et al (2022) Observations of the lower atmosphere from the 2021 WiscoDISCO campaign. *Earth Syst Sci Data* 14:2129–2145. <https://doi.org/10.5194/essd-14-2129-2022>
- Costa FD, Acevedo OC, Mombach JCM, Degrazia GA (2011) A simplified model for intermittent turbulence in the nocturnal boundary layer. *J Atmos Sci* 68:1714–1729. <https://doi.org/10.1175/2011JAS3655.1>
- Coulter RL (1990) A case study of turbulence in the stable nocturnal boundary layer. *Boundary-Layer Meteorol* 52:75–91. <https://doi.org/10.1007/BF00123179>
- Couvreur F, Bazile E, Rodier Q et al (2020) Intercomparison of large-eddy simulations of the Antarctic boundary layer for very stable stratification. *Boundary-Layer Meteorol* 176:369–400. <https://doi.org/10.1007/s10546-020-00539-4>
- Cuxart J, Holtslag AAM, Beare RJ et al (2006) Single-column model intercomparison for a stably stratified atmospheric boundary layer. *Boundary-Layer Meteorol* 118:273–303. <https://doi.org/10.1007/s10546-005-3780-1>
- Dai C, Wang Q, Kalogiros JA et al (2014) Determining boundary-layer height from aircraft measurements. *Boundary-Layer Meteorol* 152:277–302. <https://doi.org/10.1007/s10546-014-9929-z>
- Dalaudier F, Sidi C, Crochet M, Vernin J (1994) Direct evidence of “sheets” in the atmospheric temperature field. *J Atmos Sci* 51:237–248. [https://doi.org/10.1175/1520-0469\(1994\)051%3c0237:DEOITA%3e2.0.CO;2](https://doi.org/10.1175/1520-0469(1994)051%3c0237:DEOITA%3e2.0.CO;2)
- de Boer G, Lawrence D, Borenstein S et al (2016a) Uncrewed aircraft data from ERASMUS, 2014–2016. US Department of Energy ARM Data Center. <https://doi.org/10.5439/1235273>
- de Boer G, Ivey M, Schmid B et al (2016b) Unmanned platforms monitor the Arctic atmosphere. *Eos (Washington DC)*, vol 97. <https://doi.org/10.1029/2016EO046441>
- de Boer G, Ivey M, Schmid B et al (2018) A bird’s-eye view: development of an operational ARM unmanned aerial capability for atmospheric research in Arctic Alaska. *Bull Am Meteorol Soc* 99:1197–1212. <https://doi.org/10.1175/BAMS-D-17-01156.1>
- de Boer G, Borenstein S, Calmer R et al (2022) Measurements from the University of Colorado RAAVEN uncrewed aircraft system during ATOMIC. *Earth Syst Sci Data* 14:19–31. <https://doi.org/10.5194/essd-14-19-2022>
- de Boer G, Butterworth B, Elston J et al (2023) Evaluation and intercomparison of small uncrewed aircraft systems used for atmospheric research. *J Atmos Ocean Technol*. <https://doi.org/10.1175/JTECH-D-23-0067.1>
- Doddi A (2021) In situ sensing and analysis of turbulence: investigation to enhance fine-structure turbulence observation capabilities of autonomous aircraft systems
- Durst CS (1933) The breakdown of steep wind gradients in inversions. *Q J R Meteorol Soc* 59:131–136. <https://doi.org/10.1002/qj.49705924906>
- Eder F, Schmidt M, Damian T et al (2015) Mesoscale eddies affect near-surface turbulent exchange: evidence from lidar and tower measurements. *J Appl Meteorol Climatol* 54:189–206. <https://doi.org/10.1175/JAMC-D-14-0140.1>
- Fernando HJS, Weil JC (2010) Whither the stable boundary layer? *Bull Am Meteorol Soc* 91:1475–1484. <https://doi.org/10.1175/2010BAMS2770.1>
- Frehlich R, Meillier Y, Jensen ML, Balsley B (2003) Turbulence measurements with the CIRES tethered lifting system during CASES-99: calibration and spectral analysis of temperature and velocity. *J Atmos Sci* 60:2487–2495. [https://doi.org/10.1175/1520-0469\(2003\)060%3c2487:TMWTCT%3e2.0.CO;2](https://doi.org/10.1175/1520-0469(2003)060%3c2487:TMWTCT%3e2.0.CO;2)
- Fritts DC, Bizon C, Werne JA, Meyer CK (2003) Layering accompanying turbulence generation due to shear instability and gravity-wave breaking. *J Geophys Res Atmos* 108:1–13. <https://doi.org/10.1029/2002jd002406>
- Fritts DC, Wang L, Werne J (2009) Gravity wave–fine structure interactions: a reservoir of small-scale and large-scale turbulence energy. *Geophys Res Lett* 36:L19805. <https://doi.org/10.1029/2009GL039501>

- Galperin B, Sukoriansky S, Anderson PS (2007) On the critical Richardson number in stably stratified turbulence. *Atmos Sci Lett* 8:65–69. <https://doi.org/10.1002/asl.153>
- Grachev AA, Andreas EL, Fairall CW et al (2013) The critical richardson number and limits of applicability of local similarity theory in the stable boundary layer. *Boundary Layer Meteorol* 147:51–82. <https://doi.org/10.1007/s10546-012-9771-0>
- Hamilton J, de Boer G, Doddi A, Lawrence DA (2022) The DataHawk2 uncrewed aircraft system for atmospheric research. *Atmos Meas Tech* 15(22):6789–6806
- Hennemuth B, Lammert A (2006) Determination of the atmospheric boundary layer height from radiosonde and lidar backscatter. *Boundary-Layer Meteorol* 120:181–200. <https://doi.org/10.1007/s10546-005-9035-3>
- Holtslag AAM, Svensson G, Baas P et al (2013) Stable atmospheric boundary layers and diurnal cycles: challenges for weather and climate models. *Bull Am Meteorol Soc* 94:1691–1706. <https://doi.org/10.1175/BAMS-D-11-00187.1>
- Howard LN (1961) Note on a paper of John W. Miles. *J Fluid Mech* 10:509. <https://doi.org/10.1017/S0022112061000317>
- Hyun Y-K, Kim K-E, Ha K-J (2005) A comparison of methods to estimate the height of stable boundary layer over a temperate grassland. *Agric for Meteorol* 132:132–142. <https://doi.org/10.1016/j.agrformet.2005.03.010>
- Kaimal JC, Finnigan JJ (1994) Atmospheric boundary layer flows—their structure and measurement. Oxford University Press, New York
- Kantha L, Lawrence D, Luce H et al (2017) Shigaraki UAV-Radar experiment (ShUREX): overview of the campaign with some preliminary results. *Prog Earth Planet Sci* 4:19. <https://doi.org/10.1186/s40645-017-0133-x>
- Kral ST, Reuder J, Vihma T et al (2021) The innovative strategies for observations in the arctic atmospheric boundary layer project (ISOBAR) unique finescale observations under stable and very stable conditions. *Bull Am Meteorol Soc* 102:E218–E243. <https://doi.org/10.1175/BAMS-D-19-0212.1>
- Lundquist JK, Bariteau L (2015) Dissipation of turbulence in the wake of a wind turbine. *Boundary Layer Meteorol* 154:229–241. <https://doi.org/10.1007/s10546-014-9978-3>
- Mahrt L (1985) Vertical structure and turbulence in the very stable boundary layer. *J Atmos Sci* 42:2333–2349. [https://doi.org/10.1175/1520-0469\(1985\)042%3c2333:VSATIT%3e2.0.CO;2](https://doi.org/10.1175/1520-0469(1985)042%3c2333:VSATIT%3e2.0.CO;2)
- Mahrt L (1987) Grid-averaged surface fluxes. *Mon Weather Rev* 115:1550–1560. [https://doi.org/10.1175/1520-0493\(1987\)115%3c1550:GASF%3e2.0.CO;2](https://doi.org/10.1175/1520-0493(1987)115%3c1550:GASF%3e2.0.CO;2)
- Mahrt L (1999) Stratified atmospheric boundary layers. *Boundary-Layer Meteorol* 90:375–396
- Mahrt L (2014) Stably stratified atmospheric boundary layers. *Annu Rev Fluid Mech* 46:23–45. <https://doi.org/10.1146/annurev-fluid-010313-141354>
- Mahrt L, Vickers D (2003) Formulation of turbulent fluxes in the stable boundary layer. *J Atmos Sci* 60:2538–2548. [https://doi.org/10.1175/1520-0469\(2003\)060%3c2538:FOTFIT%3e2.0.CO;2](https://doi.org/10.1175/1520-0469(2003)060%3c2538:FOTFIT%3e2.0.CO;2)
- Martucci G, Matthey R, Mitev V, Richner H (2007) Comparison between backscatter lidar and radiosonde measurements of the diurnal and nocturnal stratification in the lower troposphere. *J Atmos Ocean Technol* 24:1231–1244. <https://doi.org/10.1175/JTECH2036.1>
- Medeiros LE, Fitzjarrald DR (2014) Stable boundary layer in complex terrain. Part I: linking fluxes and intermittency to an average stability index. *J Appl Meteorol Climatol* 53:2196–2215. <https://doi.org/10.1175/JAMC-D-13-0345.1>
- Medeiros LE, Fitzjarrald DR (2015) Stable boundary layer in complex terrain. Part II: geometrical and sheltering effects on mixing. *J Appl Meteorol Climatol* 54:170–188. <https://doi.org/10.1175/JAMC-D-13-0346.1>
- Meillier YP, Frehlich RG, Jones RM, Balsley BB (2008) Modulation of small-scale turbulence by ducted gravity waves in the nocturnal boundary layer. *J Atmos Sci* 65:1414–1427. <https://doi.org/10.1175/2007JAS2359.1>
- Miles JW (1961) On the stability of heterogeneous shear flows. *J Fluid Mech* 10:496. <https://doi.org/10.1017/S0022112061000305>
- Muschinski A, Wode C (1998) First in situ evidence for coexisting submeter temperature and humidity sheets in the lower free troposphere\*. *J Atmos Sci* 55:2893–2906. [https://doi.org/10.1175/1520-0469\(1998\)055%3c2893:FISEFC%3e2.0.CO;2](https://doi.org/10.1175/1520-0469(1998)055%3c2893:FISEFC%3e2.0.CO;2)
- Nakamura R, Mahrt L (2005) A study of intermittent turbulence with cases-99 tower measurements. *Boundary-Layer Meteorol* 114:367–387. <https://doi.org/10.1007/s10546-004-0857-1>
- Nappo CJ (1991) Sporadic breakdowns of stability in the PBL over simple and complex terrain. *Boundary-Layer Meteorol* 54:69–87. <https://doi.org/10.1007/BF00119413>
- Nieuwstadt FTM (1984) The turbulent structure of the stable, nocturnal boundary layer. *J Atmos Sci* 41:2202–2216. [https://doi.org/10.1175/1520-0469\(1984\)041%3c2202:TTSOTS%3e2.0.CO;2](https://doi.org/10.1175/1520-0469(1984)041%3c2202:TTSOTS%3e2.0.CO;2)

- Nuijens L, Savazzi A, de Boer G et al (2022) The frictional layer in the observed momentum budget of the trades. *Q J R Meteorol Soc.* <https://doi.org/10.1002/qj.4364>
- Ohya Y, Nakamura R, Uchida T (2008) Intermittent bursting of turbulence in a stable boundary layer with low-level jet. *Boundary Layer Meteorol* 126:349–363. <https://doi.org/10.1007/s10546-007-9245-y>
- Rohr JJ, Itsweire EC, Helland KN, Van ACW (1988) Growth and decay of turbulence in a stably stratified shear flow. *J Fluid Mech* 195:77. <https://doi.org/10.1017/S0022112088002332>
- Sandu I, Beljaars A, Bechtold P et al (2013) Why is it so difficult to represent stably stratified conditions in numerical weather prediction (NWP) models? *J Adv Model Earth Syst* 5:117–133. <https://doi.org/10.1002/jame.20013>
- Scotti RS, Corcos GM (1972) An experiment on the stability of small disturbances in a stratified free shear layer. *J Fluid Mech* 52:499–528. <https://doi.org/10.1017/S0022112072001569>
- Sorbjan Z, Grachev AA (2010) An evaluation of the flux–gradient relationship in the stable boundary layer. *Boundary-Layer Meteorol* 135:385–405. <https://doi.org/10.1007/s10546-010-9482-3>
- Steenefeld G (2012) Stable boundary layer Issues. ECMWF GABLS workshop on Diurnal cycles and the stable boundary layer 25–36
- Steenefeld GJ (2014) Current challenges in understanding and forecasting stable boundary layers over land and ice. *Front Environ Sci* 2:1–6. <https://doi.org/10.3389/fenvs.2014.00041>
- Straume AG, Koffi EN, Nodop K (1998) Dispersion modeling using ensemble forecasts compared to ETEX measurements. *J Appl Meteorol* 37:1444–1456. [https://doi.org/10.1175/1520-0450\(1998\)037%3c1444:DMUEFC%3e2.0.CO;2](https://doi.org/10.1175/1520-0450(1998)037%3c1444:DMUEFC%3e2.0.CO;2)
- Stull RB (1988) An introduction to boundary layer meteorology. Springer, Dordrecht
- Sullivan PP, Weil JC, Patton EG et al (2016) Turbulent winds and temperature fronts in large-eddy simulations of the stable atmospheric boundary layer. *J Atmos Sci* 73:1815–1840. <https://doi.org/10.1175/JAS-D-15-0339.1>
- Sun J, Lenschow DH, Burns SP et al (2004) Turbulence in nocturnal boundary layers. *Boundary-Layer Meteorol* 110:255–279
- Taylor GI (1931) Effect of variation in density on the stability of superposed streams of fluid. *Proc R Soc Lond Ser Contain Pap Math Phys Character* 132:499–523. <https://doi.org/10.1098/rspa.1931.0115>
- Tirado J, Torti AO, Butterworth BJ et al (2023) Observations of coastal dynamics during lake breeze at a shoreline impacted by high ozone. *Environ Sci Atmos* 3:494–505. <https://doi.org/10.1039/D2EA00101B>
- Tjernström M, Žagar M, Svensson G et al (2005) Modelling the Arctic boundary layer: an evaluation of six ARCMIP regional-scale models using data from the SHEBA project. *Boundary-Layer Meteorol* 117:337–381. <https://doi.org/10.1007/s10546-004-7954-z>
- Tjernström M, Balsley BB, Svensson G, Nappo CJ (2009) The effects of critical layers on residual layer turbulence. *J Atmos Sci* 66:468–480. <https://doi.org/10.1175/2008JAS2729.1>
- van de Wiel BJH, Moene AF, Steeneveld GJ et al (2007) Predicting the collapse of turbulence in stably stratified boundary layers. *Flow Turbul Combust* 79:251–274. <https://doi.org/10.1007/s10494-007-9094-2>
- van de Wiel BJH, Moene AF, Jonker HJJ et al (2012) The minimum wind speed for sustainable turbulence in the nocturnal boundary layer. *J Atmos Sci* 69:3116–3127. <https://doi.org/10.1175/JAS-D-12-0107.1>
- van den Kroonenberg AC, Martin S, Beyrich F, Bange J (2012) Spatially-averaged temperature structure parameter over a heterogeneous surface measured by an unmanned aerial vehicle. *Boundary-Layer Meteorol* 142:55–77. <https://doi.org/10.1007/s10546-011-9662-9>
- Webb EK (1970) Profile relationships: The log-linear range, and extension to strong stability. *Quarterly Journal of the Royal Meteorological Society* 96:67–90. <https://doi.org/10.1002/qj.49709640708>
- Wyngaard JC, Coté OR (1972) Cospectral similarity in the atmospheric surface layer. *Q J R Meteorol Soc* 98:590–603. <https://doi.org/10.1002/qj.49709841708>